NASA
Technical
Paper
2624

December 1986

Effect of Port Corner Geometry on the Internal Performance of a Rotating-Vane-Type Thrust Reverser

Bobby L. Berrier and
Francis J. Capone

NASA

NASA Technical Paper 2624

1986

Effect of Port Corner Geometry on the Internal Performance of a Rotating-Vane-Type Thrust Reverser

Bobby L. Berrier and
Francis J. Capone

Langley Research Center
Hampton, Virginia

NASA
National Aeronautics
and Space Administration

Scientific and Technical Information Branch

Summary

An investigation has been conducted in the static-test facility of the Langley 16-Foot Transonic Tunnel to determine the effects of reverser port geometry on the internal performance of a nonaxisymmetric rotating-vane-type thrust reverser. Thrust reverser vane positions representing a spoiled-thrust (partially deployed) position and a full-reverse-thrust (fully deployed) position were tested with each port geometry variable. The effects of upstream port corner radius and wall angle on internal performance were determined. In addition, the effect of the length of a simulated cooling liner (blunt-base step) near the reverser port entrance was investigated; five different lengths were tested. All tests were conducted with no external flow, and nozzle pressure ratio was varied from 1.2 to 5.0.

Results of this study indicate that relative to the large effect of geometric reverser vane angle, the other geometric variables investigated generally had only small effects on the thrust and efflux angle parameters. Variable angle vanes appear to provide a simple means for effective control of thrust ratio. Spoiled-thrust configurations produced significantly lower discharge coefficients than full-reverse-thrust configurations. Discharge coefficients for the spoiled-thrust configurations could be significantly increased by increasing port corner radius and/or decreasing upstream port wall angle. For configurations with a simulated cooling liner, decreasing cooling liner length increased discharge coefficient.

Introduction

The next generation of fighter aircraft will probably be required to possess a short take-off and landing (STOL) capability (refs. 1 to 5). This capability would allow the aircraft to use a greater number of airfields (which would be too short for conventional take-off and landing fighter aircraft) and also to use undamaged portions of bombed runways, taxiways, and roadways. Several studies have indicated that landing distance is the critical design requirement for STOL aircraft (refs. 6 to 8). One method which has proven to be extremely effective in reducing landing distance is thrust reversal (refs. 4, 5, and 7 to 9). In addition, once a thrust reverser is installed to meet STOL requirements, use of thrust reversing at other flight conditions has the potential to provide superior deceleration and closure rate control, steeper dive angles and lower pull-up altitude during bombing, and enhanced maneuverability (refs. 4, 5, and 9 to 12).

In recent years, many studies have been conducted to determine the weight, cooling and mechanical operation (refs. 9, 13, and 14), internal performance—both subscale (refs. 15 to 21) and full-scale (refs. 19 and 22), and installed performance (refs. 23 to 29) of thrust reverser configurations. Many of the early studies did not report on the effects of reverser deployment on weight-flow (discharge coefficient) characteristics. Nelson and Nicolai indicate in reference 11 that maintaining a constant flow area (constant discharge coefficient or effective throat area) during reverser deployment and operation is one of the primary requirements for an acceptable thrust reverser design. Of the experimental studies which provide weight-flow characteristics (refs. 16 to 21 and 27), some indicate reductions in discharge coefficient (effective throat area) of up to 40 percent when the thrust reverser is deployed. As indicated by Re and Mason in reference 20, reductions in effective throat area of only 8 percent could be sufficient to cause engine stall of a typical fighter engine at approach and landing conditions.

This paper presents the results of an experimental investigation to determine the effects of reverser port geometry on the internal performance of a nonaxisymmetric rotating-vane-type thrust reverser. This type of thrust reverser was utilized for the F-15/STOL airplane configuration of references 4, 5, 28, and 29. The investigation was conducted at static (wind-off) conditions in the static-test facility of the Langley 16-Foot Transonic Tunnel. Thrust reverser vane positions representing a spoiled-thrust (partially deployed) position and a full-reverse-thrust (fully deployed) position were tested with each port geometry variable. The effects of port corner radius and upstream port wall angle on internal performance were determined. In addition, the effect of the length of a simulated cooling liner (blunt-base step) near the reverser port entrance was investigated. Five different cooling liner lengths were tested. Nozzle pressure ratio was varied from 1.2 to 5.0 for all configurations.

Symbols

All forces (with the exception of resultant gross thrust) and angles are referred to the model centerline (body axis). A detailed discussion of the data-reduction and calibration procedures as well as definitions of forces, angles, and propulsion relationships used herein can be found in references 30 and 31.

A_t	nozzle throat area, in^2
C_d	discharge coefficient, w_p/w_i
F	measured thrust along body axis, positive in forward direction, lbf

F_i ideal gross thrust, $w_p\sqrt{\frac{R_j T_{t,j}}{g}\frac{2\gamma}{\gamma-1}\left[1-\left(\frac{p_a}{p_{t,j}}\right)^{(\gamma-1)/\gamma}\right]}$, lbf

F_N measured normal force, positive up, lbf

F_r resultant gross thrust, $\sqrt{F^2+F_N^2}$, lbf

g acceleration due to gravity, 32.174 ft/sec^2

M_j jet Mach number based on static pressure on upstream port corner wall

NPR nozzle pressure ratio, $p_{t,j}/p_a$

p local static pressure, psi

p_a ambient pressure, psi

$p_{t,j}$ jet total pressure, psi

R port corner radius, in.

R_j jet gas constant, 53.36 ft/°R

$T_{t,j}$ jet total temperature, °R

w_i ideal weight-flow rate, lbf/sec

w_p measured weight-flow rate, lbf/sec

x axial distance from upstream port corner to base of simulated cooling liner (see fig. 4(c)) positive downstream, in.

y_1, y_2 lateral distances from nozzle sidewall to static-pressure orifice (see fig. 7), in.

z_1, z_2 vertical distances from bottom of port entrance (WL = 1.39) to static-pressure orifice (see fig. 7), in.

γ ratio of specific heats, 1.3997 for air

δ resultant reverser efflux angle; for $\theta \leq 90°$, $\delta = \tan^{-1}(F_N/F)$, deg; for $\theta > 90°$, $\delta = \tan^{-1}(F_N/F) - 180°$, deg

θ geometric reverser vane angle measured from horizontal reference line, positive in counterclockwise direction, deg

σ geometric angle of upstream port passage wall measured from horizontal reference line, positive in counterclockwise direction, deg

Abbreviations:

FS fuselage station (location described by distance in inches from FS 0.00; see fig. 1(a))

STOL short take-off and landing

WL water line (location described by distance in inches from WL 0.00; see fig. 3(b))

Configuration designation:

Number/Letter Number is the value of the geometric reverser vane angle in degrees, and letter is the letter designation of the port corner configuration (see fig. 4)

Apparatus and Methods

Static-Test Facility

This investigation was conducted in the static-test facility of the Langley 16-Foot Transonic Tunnel. Testing is conducted in a large room where the jet from a simulated single-engine propulsion system exhausts to the atmosphere through a large open doorway. A control room is remotely located from the test area, and a closed-circuit television is used to observe the model when the jet is operating. The static-test facility has an air control system which is similar to that of the 16-Foot Transonic Tunnel and includes valving, filters, and a heat exchanger to maintain the jet flow at constant stagnation temperature. The air system utilizes the same clean dry-air supply as that used in the 16-Foot Transonic Tunnel (ref. 30).

Single-Engine Propulsion Simulation System

A sketch of the single-engine air-powered nacelle model on which various thrust reverser port configurations were mounted is presented in figure 1 with a typical configuration attached. Figure 2 presents a photograph of a typical hardware installation.

An external high-pressure air system provided a continuous flow of clean dry air at a controlled temperature of about 540°R. This high-pressure air was varied up to about 75 psi during jet simulation. The pressurized air was supplied by six air lines through a dolly-mounted support strut and fed into a high-pressure plenum chamber. The air was

then discharged perpendicularly into the model low-pressure plenum through eight multiholed sonic nozzles equally spaced around the high-pressure plenum. (See fig. 1.) This airflow system was designed to minimize any forces imposed by the transfer of axial momentum as the air passed from the nonmetric high-pressure plenum to the metric (attached to the balance) low-pressure plenum. Two flexible metal bellows sealed the air system (between the metric and the nonmetric model parts) and compensated for axial forces caused by pressurization. The low-pressure air then passed from the circular low-pressure plenum through a circular-to-rectangular transition section, a rectangular choke plate, and a rectangular instrumentation section, which were common for all nozzles tested. The instrumentation section had a ratio of flow path width to height of 1.437 and was identical in geometry to the nozzle airflow entrance (nozzle connect station). All nozzle configurations were attached to the instrumentation section at fuselage station 41.13.

Model and Port Description

Figure 3 presents sketches showing the assembly of the thrust reverser test hardware downstream of FS 41.13 and details of the thrust spoiler vane box ($\theta = 60°$) and full-reverse-thrust vane box ($\theta = 135°$). Geometric details of the various port corner configurations tested are shown in the sketches of figure 4, and photographs of several reverser port configurations are shown in figure 5. The test hardware downstream of FS 41.13 essentially represents the top half (reverser ports on top) of a nonaxisymmetric nozzle thrust reverser installation. (See figs. 3(a) and 3(b).) Only the top reverser ports were simulated in order to obtain a direct measurement of normal force and thus determine resultant reverser efflux angle (see the definition of δ in the "Symbols" section); simulation of the complete reverser (reverser ports on top and bottom) would result in a net normal force of zero. The nozzle internal, or duct, geometry was rectangular in cross section and had a constant flow path width of 4.00 in. The duct internal flow area just upstream of the port corner (FS 45.93) was sized to produce an internal Mach number between 0.2 and 0.3, which is typical of full-scale hardware. A splitter plate (see fig. 3(b)) inside the model was used to represent the horizontal plane of flow symmetry (if the model had been a complete configuration with top and bottom ports). The splitter plate provides a more realistic turning of the flow by the blocker (downstream port wall) than if the blocker wall extended completely to the lower nozzle wall. All reverser configurations tested had a simulated reverser blocker angle of 83°.

A vane box was located directly on top of the port passage, and the vane box center wall divided the port into two reverser passages. (See fig. 5(a).) No attempt was made during the current test to turn (splay) the reverser flow laterally. Data on lateral turning of the exhaust flow for a similar configuration are contained in reference 21. For operational full-scale hardware, the vanes contained in the vane box are fully variable between vane angles of 0° (stowed reverser) to 135° (fully deployed reverser). Vane angles between 0° and 90° represent spoiled-thrust (forward-thrust component) settings, and vane angles between 90° and 135° represent reverse-thrust settings. As shown in figure 3, two vane angles, 60° and 135°, were tested during the current investigation. Both vane settings were tested with each port corner geometry investigated. The vane box center wall (see fig. 3(d)) included an actuator fairing which extended downward into the port passage. On the full-scale hardware, the actuator fairing covers the actuators and mechanisms necessary to vary the vane angle. To determine the effect of this actuator fairing on reverser performance, it was removed for one vane box configuration with $\theta = 135°$. It can be noted from the sketch of figure 3(e) that vane geometry was slightly different for the vane boxes with $\theta = 60°$ and $\theta = 135°$. The vane boxes were built at separate times, and the reverser design changed in the interim. It is believed that the indicated differences had no effect on the results, especially since there are few direct comparisons between the $\theta = 60°$ and $\theta = 135°$ data sets.

Two different types of port corners were tested during this investigation, one set without a simulated cooling liner, denoted port corners A through G (see figs. 4(a) and 4(b)), and one set with a simulated cooling liner, denoted port corners H through L. (See fig. 4(c).) Port corner configuration M (fig. 4(c)) was used in both the port corner and simulated cooling liner comparisons. It represents both a sharp radius port corner configuration and a cooling liner configuration which is beveled to fair into the upstream port wall and eliminate the blunt-base region.

Port corners A through G were used to investigate the effects of corner radius ($R = 0.064$ to 0.163 in.) and upstream port passage wall angle ($\sigma = 90.00°$ to 122.33°) on reverser performance. A comparison of port corner geometry for port corners A through G is shown in figure 6. Port corner M provides a limiting case of $R = 0.000$ in. (sharp corner) for the series of port corners with $\sigma = 122.33°$ (C, D, and E).

Port corners H through L were used to investigate the effects on reverser performance of a simulated cooling liner near the reverser port entrance. For full-scale hardware, a cooling liner is used to contain low-

energy cool (lower temperature than the jet) airflow between the liner (and hot exhaust flow) and the nozzle walls. Since the model had no provision for a second controlled airflow, the cooling liner was simulated by a flat plate with a rearward-facing step, or blunt base. (See fig. 4(c).) The low-energy cooling flow which would exhaust from this base was not simulated. The upstream port passage wall angle σ was held at a constant value of 122.33° for these port corner configurations. The length of the simulated cooling liner was varied from 0.115 in. longer than the port corner (port corner H) to 0.047 in. shorter than the port corner (port corner L). Port corner M represents a configuration with the simulated cooling liner cut off at an angle equal to the port passage wall angle rather than at 90° (blunt base).

Instrumentation

A six-component strain-gauge balance was used to measure the forces and moments on the model. Jet total pressure was measured at a fixed station in the instrumentation section by means of a four-probe rake through the upper surface, a three-probe rake through the side, and a two-probe rake through the corner. (See fig. 1.) A thermocouple was also positioned in the instrumentation section to measure the jet total temperature. Weight flow of the high-pressure air supplied to the simulated thrust reverser was determined from a calibrated choked-venturi located in the air line external to the model. Two static-pressure orifices were located on the upstream wall of the port passage for most port corner configurations tested; the locations of these static-pressure orifices are given in figure 7.

Data Reduction

Approximately 50 frames of data, taken at a rate of 10 frames per second, were used for each data point; average values were used in the computations. With the exception of resultant gross thrust F_r, all data in this report are referenced to the model centerline. Four basic performance parameters are used in the presentation of results; they are internal thrust ratio F/F_i, resultant gross thrust ratio F_r/F_i, discharge coefficient C_d, and resultant reverser efflux angle δ.

Internal thrust ratio F/F_i is the ratio of the actual measured nozzle thrust along the body axis to the ideal nozzle thrust. Ideal thrust F_i is based on measured weight flow w_p, jet total pressure $p_{t,j}$, and jet total temperature $T_{t,j}$. (See the section "Symbols.") The balance axial-force measurement, from which the actual nozzle thrust F is subsequently obtained, is initially corrected for model weight tares and balance interactions. Although the bellows arrangement in the air pressurization system was designed to eliminate pressure and momentum interactions with the balance, small bellows tares on the six balance components still exist. These tares result from a small pressure difference between the ends of the bellows when air system internal velocities are high and from small differences in the forward and aft bellows spring constants when the bellows are pressurized. These bellows tares were determined by running standard axisymmetric calibration nozzles with known performance over a range of expected longitudinal forces and moments. The resulting tares were then applied to the balance data to obtain thrust along the body axis F. The procedure for computing the bellows tares is discussed in detail in reference 30.

The resultant thrust ratio F_r/F_i is the resultant gross thrust divided by the ideal thrust. Resultant gross thrust is obtained from the measured axial (thrust along the body axis) and normal components of the jet resultant force. For the current test, the side component of the jet resultant force was zero, since the exhaust flow was not turned laterally. From the definitions of F and F_r, it is obvious that the thrust along the body axis F includes losses which result from turning the exhaust vector away from the axial direction, whereas resultant gross thrust F_r does not.

Nozzle discharge coefficient C_d is the ratio of measured weight flow to ideal weight flow where ideal weight flow (in lbf/sec) is computed from equation (1) or (2), depending on the value of NPR. If NPR ≤ 1.89 (unchoked nozzle flow)

$$w_i = A_t p_{t,j} \left(\frac{1}{\text{NPR}}\right)^{1/\gamma} \sqrt{\frac{2g}{T_{t,j} R_j} \frac{\gamma}{(\gamma - 1)} \left[1 - \left(\frac{1}{\text{NPR}}\right)^{(\gamma-1)/\gamma}\right]} \quad (1)$$

If NPR > 1.89 (choked nozzle flow)

$$w_i = A_t p_{t,j} \left(\frac{2}{\gamma + 1}\right)^{(\gamma+1)/2(\gamma-1)} \sqrt{\frac{\gamma g}{T_{t,j} R_j}} \quad (2)$$

Nozzle discharge coefficient reflects the ability of a nozzle to pass weight flow and is reduced by any momentum and vena contracta losses (effective throat area less than A_t). Nozzle throat area A_t is the measured minimum area through the vane passages.

Resultant reverser efflux angle δ is the angle at which the reverser vanes turn the exhaust flow from the axial direction. As indicated in the "Symbols"

section, determination of δ requires the measurement of axial force (thrust along the body axis) and normal force. For this reason, the reverser model used in the current investigation simulated only the top reverser ports. Simulation of top and bottom reverser ports would have resulted in a mutual cancellation of normal force (net value of approximately zero).

Presentation of Results

The results of this investigation are presented graphically in figures 8 to 12. An index relating thrust reverser configurations to force, discharge coefficient, and static-pressure ratio data is given in table I. Summary and comparison data are plotted in the following figures:

Results and Discussion

Thrust and Efflux Angle Performance

The effects of port corner geometry and reverser vane angle on internal thrust ratio F/F_i, resultant gross thrust ratio F_r/F_i, and resultant reverser efflux angle δ (also discharge coefficient, but these effects will be discussed later) are presented in figures 8 through 12 as a function of nozzle pressure ratio. Relative to the large effect of geometric reverser vane angle θ, the other model geometric variables generally had only small effects on the thrust and efflux angle parameters. This result is more clearly shown in figure 13, which compares most of the configurations tested at constant NPR. Resultant reverser efflux angle δ in particular showed little sensitivity to the model geometric variables tested except for geometric reverser vane angle. This behavior might be expected, since the intent of the current thrust reverser design was to use the reverser vanes (geometric vane angle) to set resultant reverser efflux angle (and thus the level of thrust spoiling or reversing obtained). Any effects of varying internal port geometry (upstream of the reverser vanes) on resultant reverser vane angle δ are probably minimized by the large effects of the downstream reverser vanes.

The effect of geometric vane angle on resultant reverser efflux angle is summarized on the right side of figure 13. Ideally, resultant reverser efflux angle should have the same magnitude (but opposite sign because of the definition of δ) as the geometric reverser vane angle. As shown in figure 13, the absolute value of measured resultant reverser efflux angle was always within 12° of the geometric reverser vane angle. For the spoiled-thrust ($\theta = 60°$) configurations, the desired value of $\delta = -60°$ was generally not obtained for NPR > 2.0 (measured values ranged from $-53°$ to $-59°$ for NPR from 3.0 to 5.0), probably because the exhaust flow is overexpanded through the aft port passage. As shown in figure 3(b), configurations with $\theta = 60°$ had little exhaust flow containment downstream of the aft port passage. Thus, the exhaust flow was free to expand in an aft direction from this port passage, and less than desired reverser efflux angles could be produced. For the full-reverse-thrust ($\theta = 135°$) configurations, the desired level of $\delta = -135°$ was exceeded for all configurations and test conditions investigated. This better than expected performance can be explained by the fact that each passage through the vanes can be viewed as an individual nonaxisymmetric single-expansion-ramp nozzle with its centerline rotated at an angle equal to θ. As shown in references 15 and 16, single-expansion-ramp nozzles tend to produce a negative thrust vector angle (i.e., to pull exhaust flow toward the external expansion ramp) at low NPR values (NPR less than that required for full expansion on the ramp). For the full-reverse-thrust configurations ($\theta = 135°$), a negative thrust vector angle for each vane passage would tend to increase the magnitude of the resultant reverser efflux angle to a value greater than the geometric reverser vane angle, as shown in the following sketch:

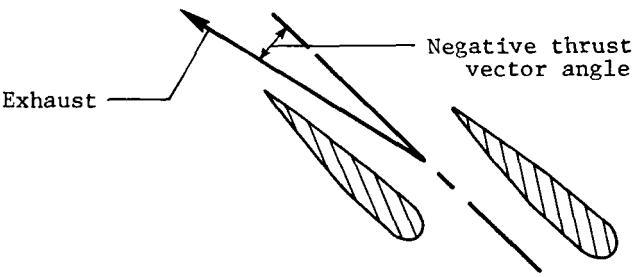

At higher nozzle pressure ratios, thrust vector angles of single-expansion-ramp nozzles tend to become positive and increase with NPR. (See ref. 16.) Thus, at NPR values greater than those tested in the current investigation, the magnitude of the resultant reverser efflux angle is expected to be less than that of the geometric vane angle, as indicated by the results reported in references 18 and 27.

The effect of geometric vane angle on internal thrust ratio is summarized on the left side of figure 13. Internal thrust ratio levels obtained during the current investigation were very close to those which can be predicted from the geometric reverser vane angle. Because of this result, variable angle reverser vanes appear to provide a simple means for effective control of thrust ratio. Reverser vane angles up to 90° would provide controlled levels of spoiled thrust (reduced forward-thrust levels but with the engine "spooled up"), which would be useful during the approach flight segment. Reverser vane angles greater than 90° would provide controlled levels of reverse thrust, which would be used for deceleration during ground roll. The variable angle feature provided by the vanes would also be useful in tailoring the reverse-thrust exhaust flow patterns to prevent engine exhaust gas ingestion as ground speed is reduced (ref. 5). Reverse-thrust levels at $\theta = 135°$ were slightly higher than would be predicted at NPR > 2.0. The reason for the increased reverse-thrust level at this condition is probably the single-expansion-ramp nozzle effect on resultant reverser efflux angle, which was discussed previously.

Discharge Coefficient Performance

Effect of NPR. The effect of nozzle pressure ratio on nozzle discharge coefficient C_d is shown in figures 8 through 12 for all configurations tested. For nozzle pressure ratios greater than 1.89 (NPR for choked nozzle flow when air is used as the exhaust), the discharge coefficient of the configurations with $\theta = 135°$ was essentially independent of NPR. The static pressures measured on the upstream port passage wall (of the configurations with $\theta = 135°$) are also nearly independent of NPR for NPR > 1.89. (See figs. 9 to 12.) Although the configurations with $\theta = 135°$ represent a fully deployed thrust reverser, these results are typical of forward-thrust cruise-type nozzle configurations (see ref. 18) and indicate a well-formed stable throat which does not vary in location or area as NPR varies. On the other hand, discharge coefficients of the configurations with $\theta = 60°$ generally increase with increasing NPR and generally do not become independent of NPR until a nozzle pressure ratio between 3.0 and 5.0 is reached. Similarly, static-pressure ratios on the upstream port wall generally become independent of NPR for only the higher values of nozzle pressure ratio. These results indicate that the reverser port throat location or the effective throat area or both are probably varying as nozzle pressure ratio increases.

Effect of actuator fairing. Figure 8 shows the effect on discharge coefficient of an actuator fairing which extends into the port passage below the center vane support beam. Removing the actuator fairing decreased nozzle discharge coefficient by about 3 to 4 percent. A possible explanation for the beneficial effect of the actuator fairing on discharge coefficient is that the fairing acts as a guide vane for the exhaust flow leading into the vane passages. Without the actuator fairing, the exhaust flow encounters the blunt face of the center vane support beam near the entrance to the vane passages. (See fig. 3(b).)

Effect of geometric reverser vane angle. The effect of geometric reverser vane angle on discharge coefficient can be seen by comparing the data for $\theta = 60°$ and $\theta = 135°$, shown in summary figures 14 and 15. This comparison indicates that geometric vane angle had a major impact on nozzle discharge coefficient. The configurations with $\theta = 60°$ had 8 to 31 percent lower discharge coefficients than the configurations with $\theta = 135°$, depending on port geometry and nozzle pressure ratio. The large decrease in discharge coefficient for the configurations with $\theta = 60°$ is probably caused by a reduction in effective throat area resulting from the close proximity of the leading edge of the most upstream vane to the upstream port wall when the reverser geometric vane angle is rotated to 60°. (See fig. 3(b).) In this case, the exhaust flow may choke at this point rather than at the desired location in the vane passage and result in reduced throat area. Of course, as geometric vane angle is increased, the distance between the vane leading edge and the upstream port wall increases, and throat location (for the upstream vane passage) would shift back to the desired location in the vane passage. Depending on the magnitude of the effective throat area change, large increases in nozzle discharge coefficient may result. This conclusion is supported by the static-pressure ratio data presented in figures 9 through 12. Static-pressure ratios measured on the configurations with $\theta = 60°$ are generally lower than those measured on the configurations with $\theta = 135°$. As indicated in the right-hand margin of these figures, lower static-pressure ratios indicate higher internal jet Mach numbers and rapid acceleration of the exhaust flow along the upstream port wall. Several of the configurations with $\theta = 60°$ have nearly sonic flow ($M_j = 1.0$) at the uppermost pressure orifice (orifice 2, which is closer to the vane passages) at the highest nozzle pressure ratios tested.

Effect of upstream port corner radius and wall angle. The effects of upstream port wall geometry on discharge coefficient are summarized in figure 14 for several nozzle pressure ratios. As shown in this figure, the spoiled-thrust configurations ($\theta = 60°$) were much more sensitive than the reverse-thrust configu-

rations (θ – 135°) to upstream port wall geometry. Even so, discharge coefficient for all configurations, including the configurations with $\theta = 135°$ (except for $R = 0.163$ in.), was increased by increasing port corner radius and/or decreasing upstream port wall angle. A possible explanation for the higher sensitivity of the configurations with $\theta = 60°$ to changes in the upstream port wall geometry is that these configurations probably have the upstream termination of the sonic line (throat of forward passage) located on the upstream port wall rather than in the vane passage, as discussed previously. Increasing port corner radius generally decreases the exhaust flow velocity leading into the port passage (see fig. 10) and tends to reduce the tendency of the configurations with $\theta = 60°$ to choke in the port passage rather than in the vane passages. Previous studies have shown that a larger corner radius not only tends to increase the discharge coefficient for reverser configurations (see ref. 20) but also for forward-thrust (cruise) nozzle configurations. (See ref. 32.) Decreasing upstream port wall angle not only reduces the exhaust flow velocity in the port passage (compare static-pressure ratio data of figs. 9, 10, and 11) but also physically increases the distance between the upstream vane ($\theta = 60°$) and upstream port wall. (See fig. 6.) Both of these effects would tend to increase nozzle discharge coefficient by either increasing effective throat area or actual physical throat area.

Effect of simulated cooling liner location. Most engine tailpipes (located immediately upstream of the reverser ports) require a cooling liner to retain cool air next to the engine wall to prevent excessive engine tailpipe and case temperatures. The current test investigated the effect of cooling liner length on reverser performance, and the results on discharge coefficient are summarized in figure 15. The simulated cooling liner consisted of flat plates of various lengths mounted to the bottom of the upstream port corner. (See fig. 4(c).) Except for port corner M, which had an angled base (angle equal to the upstream port wall angle), the simulated cooling liners had blunt bases with no base bleed. In an actual engine, engine cooling flow would exit from the base; it is believed that cooling flow from the base would tend to increase effective cooling liner length. Reducing simulated cooling liner length reduces exhaust flow velocity on the upstream port wall (see fig. 12) and increases nozzle discharge coefficient (see fig. 15) for all NPR values tested. The angled-base simulated cooling liner (port corner M), which was also included in the parametric study of port corner radius (see data for $R = 0.0$ in fig. 14), results in a decrease in discharge coefficient from those measured for the blunt-base configurations. The effect of cooling flow exiting from the angled base is not known, but it is believed that it could reduce some of the discharge coefficient loss.

Conclusions

An investigation has been conducted in the static-test facility of the Langley 16-Foot Transonic Tunnel to determine the effects of reverser port geometry on the internal performance of a nonaxisymmetric rotating-vane-type thrust reverser. Thrust reverser vane positions representing a spoiled-thrust (partially deployed) position and a full-reverse-thrust (fully deployed) position were tested with each port geometry variable. The effects of upstream port corner radius and wall angle on internal performance were determined. In addition, the effect of the length of a simulated cooling liner (blunt-base step) near the reverser port entrance was investigated; five different lengths were tested. All tests were conducted with no external flow, and nozzle pressure ratio was varied from 1.2 to 5.0. Results of this study indicate the following conclusions:

1. Relative to the large effect of geometric reverser vane angle, the other geometric variables tested generally had only small effects on reverser thrust ratio and resultant reverser efflux angle. For thrust reverser designs which use vanes located in the reverser port, variable angle vanes provide a simple means for effective control of thrust ratio.
2. The spoiled-thrust configurations (geometric vane angle of 60°) had discharge coefficients up to 31 percent lower than those of the full-reverse-thrust configurations (geometric vane angle of 135°). This drop in discharge coefficient was probably caused by a reduction in effective throat area resulting from the close proximity of the upstream vane leading edge to the upstream port wall. Significant increases in discharge coefficient were obtained on the spoiled-thrust configurations by increasing port corner radius and/or decreasing upstream port wall angle. Both of these actions reduced exhaust flow velocity in the port passage leading into the vane passages.
3. For nozzle pressure ratios above 1.89, discharge coefficient of the full-reverse-thrust configurations was essentially independent of nozzle pressure ratio. These results indicate a well-formed and stable throat location. However, discharge coefficient values for the spoiled-thrust configurations tended to increase with increasing nozzle pressure ratio and indicate a varying throat location and size.
4. Addition of an actuator fairing to the bottom of the center vane support beam increased discharge coefficient.

5. For configurations with a simulated cooling liner near the reverser port corner, reducing the length of the simulated cooling liner increased discharge coefficient.

NASA Langley Research Center
Hampton, VA 23665-5225
September 3, 1986

References

1. Kostelnik, Michael; and Schull, Dunell V.: Evolving the Advanced Tactical Fighter Concept. *Cockpit*, Soc. Exp. Test Pilots, Apr./May/June 1985, pp. 4–17.
2. Richey, G. K.; Surber, L. E.; and Berrier, B. L.: Airframe-Propulsion Integration for Fighter Aircraft. AIAA-83-0084, Jan. 1983.
3. Lind, G. W.; Fletcher, J.; Kirshbaum, N.; Krepski, R.; Bourbin, M.; Protopapas, J.; Read, J.; Giesler, W.; Burhans, W.; and Ciminera, V.: *V/STOL Technology Requirements for Future Fighter Aircraft.* AFWAL-TR-80-3153, U.S. Air Force, Dec. 1980. (Available from DTIC as AD B057 122L.)
4. Selegan, David R.: STOL and Maneuver Technology Program. *Powered Lift Systems Plus an Overview of the JVX Program*, SP-555, Soc. Automot. Eng., Inc., Dec. 1983, pp. 1–7. (Available as SAE Paper 831425.)
5. Mello, J. F.; and Kotansky, D. R.: Aero/Propulsion Technology for STOL and Maneuver. AIAA-85-4013, Oct. 1985.
6. Curry, Steven G.; Barnes, G. Ray; Jones, Thomas J.; and Hartill, William R.: Exhaust Nozzle Concepts for STOL Tactical Aircraft. AIAA-83-1226, June 1983.
7. Krepski, Robert E.; and Hudson, Raymond E., Jr.: STOL Capability Impact on Advanced Tactical Aircraft Design. AIAA-81-2617, Dec. 1981.
8. Blackman, J. P.; and Eigenmann, M. F.: Axisymmetric Approach and Landing Thrust Reversers. AIAA-81-1650, Aug. 1981.
9. *F-15 2-D Nozzle System Integration Study. Volume I—Technical Report.* NASA CR-145295, 1978.
10. Hiley, P. E.; Wallace, H. W.; and Booz, D. E.: Study of Non-Axisymmetric Nozzles Installed in Advanced Fighter Aircraft. AIAA Paper No. 75-1316, Sept.–Oct. 1975.
11. Nelson, B. D.; and Nicolai, L. M.: Application of Multi-Function Nozzles to Advanced Fighters. AIAA-81-2618, Dec. 1981.
12. Skow, Andrew M.; Hamilton, William L.; and Taylor, John H.: Advanced Fighter Agility Metrics. AIAA-85-1779, Aug. 1985.
13. Stevens, H. L.: *F-15/Nonaxisymmetric Nozzle System Integration Study Support Program.* NASA CR-135252, 1978.
14. Bergman, D.; Mace, J. L.; and Thayer, E. B.: Non-Axisymmetric Nozzle Concepts for an F-111 Test Bed. AIAA Paper No. 77-841, July 1977.
15. Capone, Francis J.: *Static Performance of Five Twin-Engine Nonaxisymmetric Nozzles With Vectoring and Reversing Capability.* NASA TP-1224, 1978.
16. Re, Richard J.; and Berrier, Bobby L.: *Static Internal Performance of Single Expansion-Ramp Nozzles With Thrust Vectoring and Reversing.* NASA TP-1962, 1982.
17. Leavitt, Laurence D.; and Re, Richard J.: *Static Internal Performance Characteristics of Two Thrust-Reverser Concepts for Axisymmetric Nozzles.* NASA TP-2025, 1982.
18. Re, Richard J.; and Leavitt, Laurence D.: *Static Internal Performance Including Thrust Vectoring and Reversing of Two-Dimensional Convergent-Divergent Nozzles.* NASA TP-2253, 1984.
19. Romine, B. M., Jr.; and Johnson, W. A.: Performance Investigation of a Fan Thrust Reverser for a High By-Pass Turbofan Engine. AIAA-84-1178, June 1984.
20. Re, Richard J.; and Mason, Mary L.: Port Geometry Effects on Thrust Reverser Static Performance. AIAA-85-1345, July 1985.
21. Leavitt, Laurence D.; and Burley, James R., II: *Static Internal Performance of a Single-Engine Nonaxisymmetric-Nozzle Vaned-Thrust-Reverser Design With Thrust Modulation Capabilities.* NASA TP-2519, 1985.
22. McLafferty, George H.; and Peterson, Jeffrey L.: Results of Tests of a Rectangular Vectoring/Reversing Nozzle on an F100 Engine. AIAA-83-1285, June 1983.
23. Hiley, P. E.; Kitzmiller, D. E.; and Willard, C. M.: Installed Performance of Vectoring/Reversing Nonaxisymmetric Nozzles. AIAA Paper No. 78-1022, July 1978.
24. Maiden, Donald L.; and Mercer, Charles E.: *Performance Characteristics of a Single-Engine Fighter Model Fitted With an In-Flight Thrust Reverser.* NASA TN D-6460, 1971.
25. Capone, Francis J.; and Berrier, Bobby L.: *Investigation of Axisymmetric and Nonaxisymmetric Nozzles Installed on a 0.10-Scale F-18 Prototype Airplane Model.* NASA TP-1638, 1980.
26. Pendergraft, Odis C., Jr.; and Bare, E. Ann: *Effect of Nozzle and Vertical-Tail Variables on the Performance of a Three-Surface F-15 Model at Transonic Mach Numbers.* NASA TP-2043, 1982.
27. Carson, George T., Jr.; Capone, Francis J.; and Mason, Mary L.: *Aeropropulsive Characteristics of Nonaxisymmetric-Nozzle Thrust Reversers at Mach Numbers From 0 to 1.20.* NASA TP-2306, 1984.
28. Banks, Daniel W.; and Paulson, John W., Jr.: Approach and Landing Technologies for STOL Fighter Configurations. *J. Aircr.*, vol. 22, no. 4, Apr. 1985, pp. 277–282.
29. Banks, Daniel W.; Quinto, P. Frank; and Paulson, John W., Jr.: *Thrust-Induced Effects on Low-Speed Aerodynamics of Fighter Aircraft.* NASA TM-83277, 1982.
30. Peddrew, Kathryn H., compiler: *A User's Guide to the Langley 16-Foot Transonic Tunnel.* NASA TM-83186, 1981.
31. Mercer, Charles E.; Berrier, Bobby L.; Capone, Francis J.; Grayston, Alan M.; and Sherman, C. D.: *Computations for the 16-Foot Transonic Tunnel—NASA, Langley Research Center.* NASA TM-86319, 1984.
32. Mason, Mary L.; Putnam, Lawrence E.; and Re, Richard J.: *The Effect of Throat Contouring on Two-Dimensional Converging-Diverging Nozzles at Static Conditions.* NASA TP-1704, 1980.

Table I. Index to Data Figures

Port corner	Actuator fairing	σ, deg	R, in.	x, in.	Figure for — $\theta = 135°$	Figure for — $\theta = 60°$
A	Removed	118.56	0.163		8(a)	
A	On	118.56	.163		8(a)	8(b)
B	↓	117.35	.125		9(a)	9(b)
C		122.33	.064		10(a)	10(b)
D		122.33	.125		10(a)	10(b)
E		122.33	.163		10(a)	10(b)
F		117.35	.163		9(a)	9(b)
G		90.00	.125		11(a) and (b)	11(a) and (b)
H		122.33	.000	0.115	12(a)	12(b)
I		↓	↓	.075	↓	↓
J				.055		
K				.015		
L				−.047		
M	↓	↓	↓	.095	10(a)	10(b)

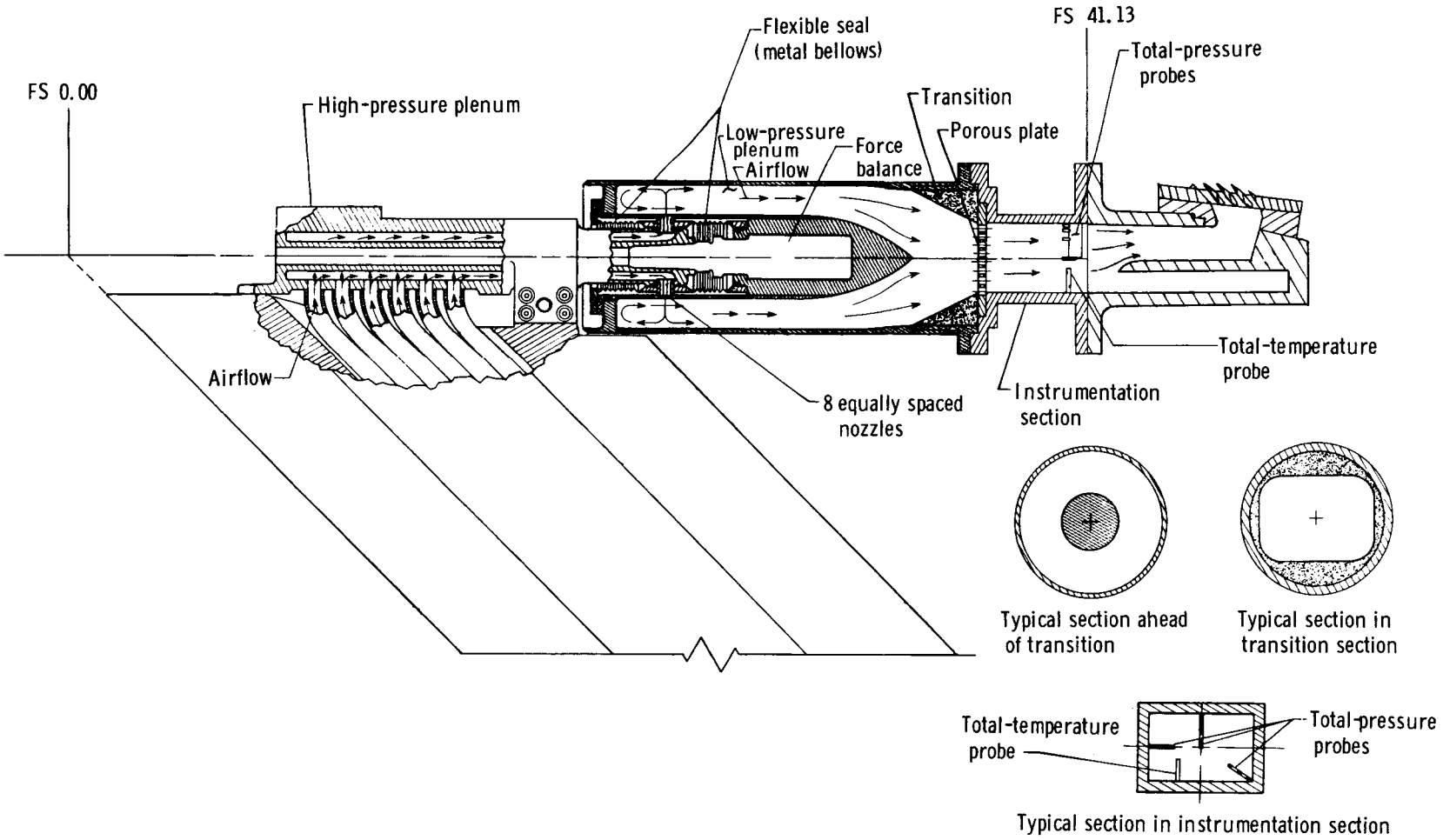

(a) Air-powered nacelle test apparatus.

Figure 1. Air-powered nacelle with port model installed and schematic of nonmetric-to-metric air transfer system. All dimensions are in inches unless otherwise indicated.

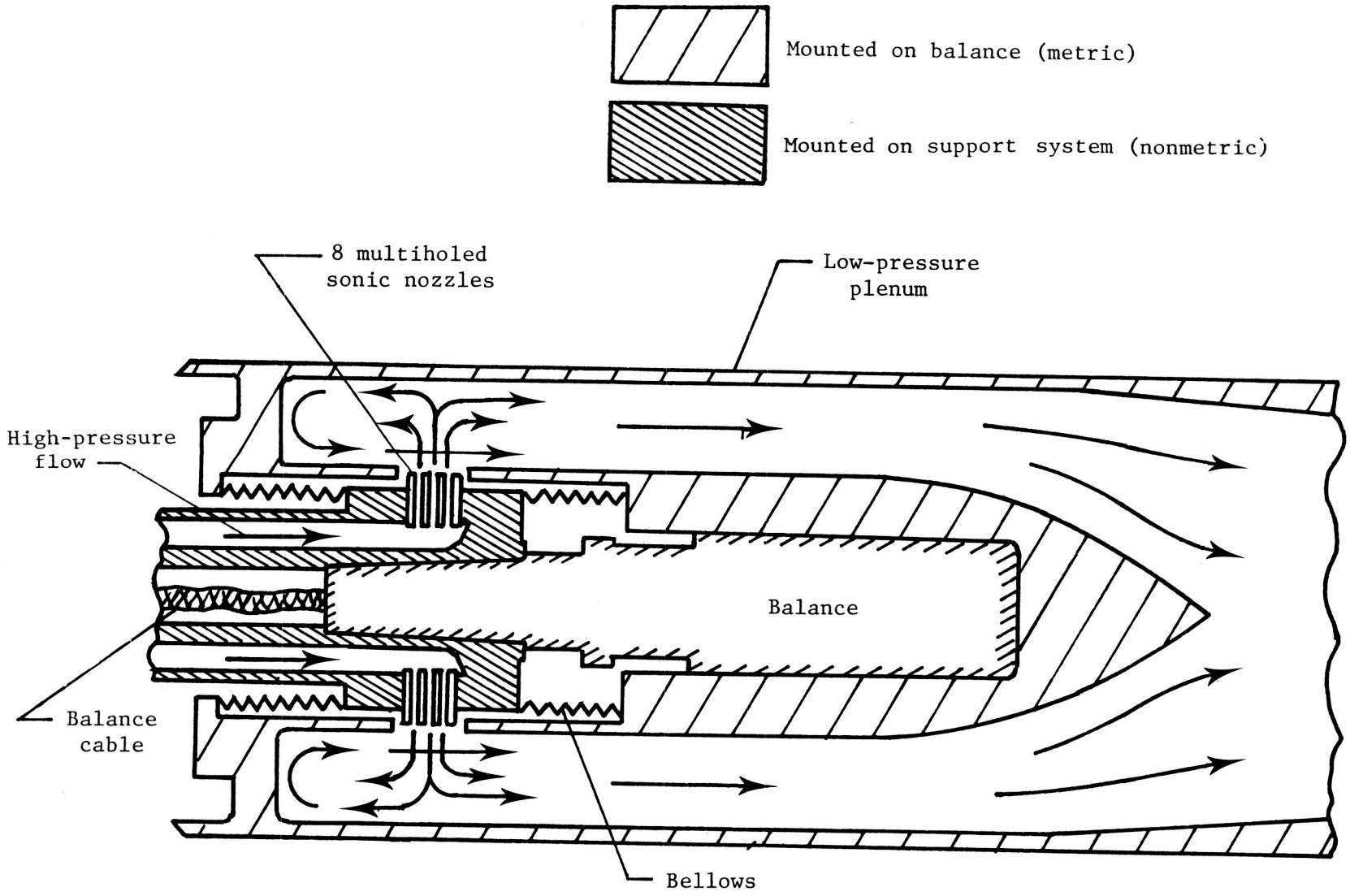

(b) Schematic cross section of flow transfer system.

Figure 1. Concluded.

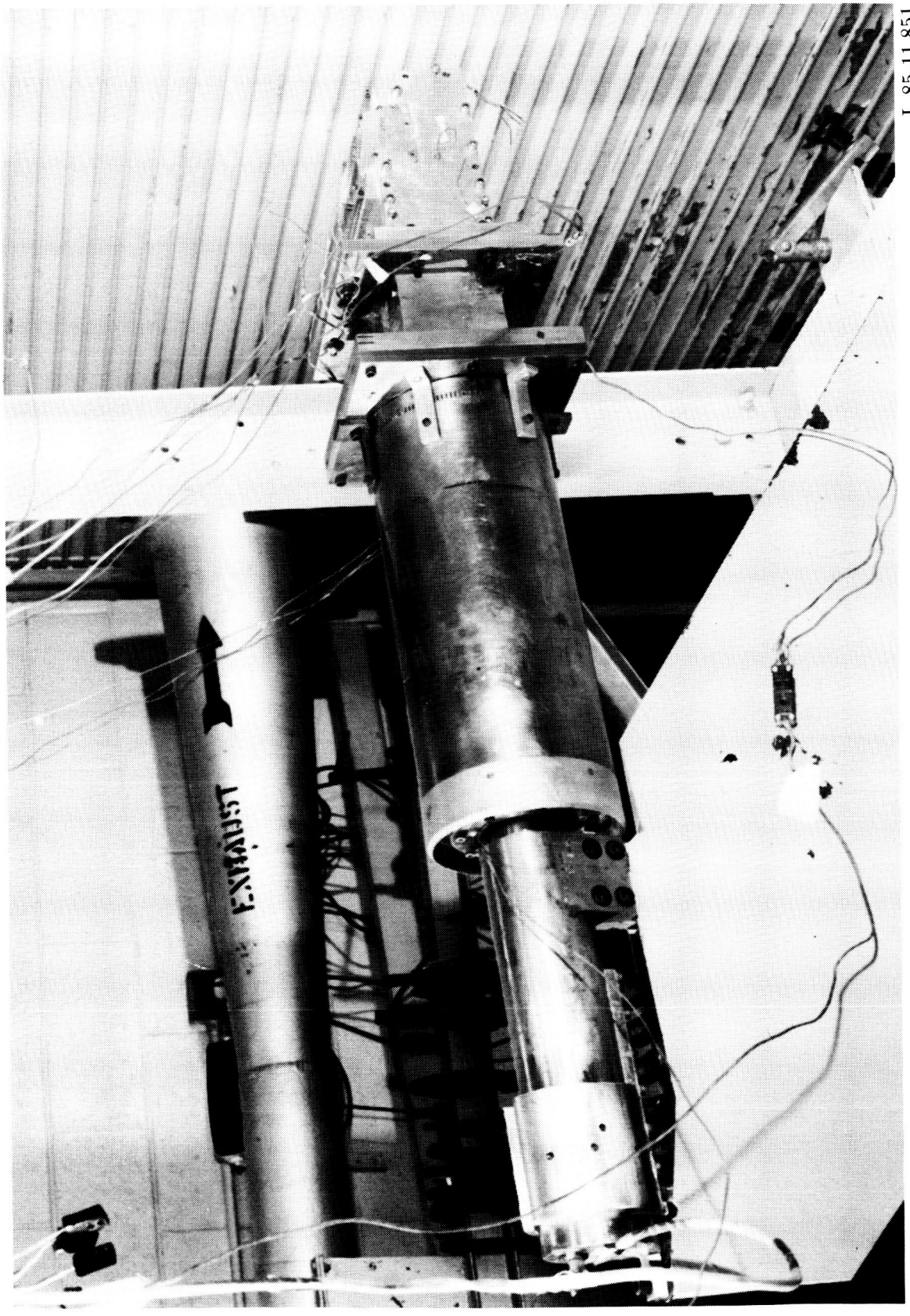

L-85-11,851

Figure 2. Propulsion simulation system with reverser port model installed.

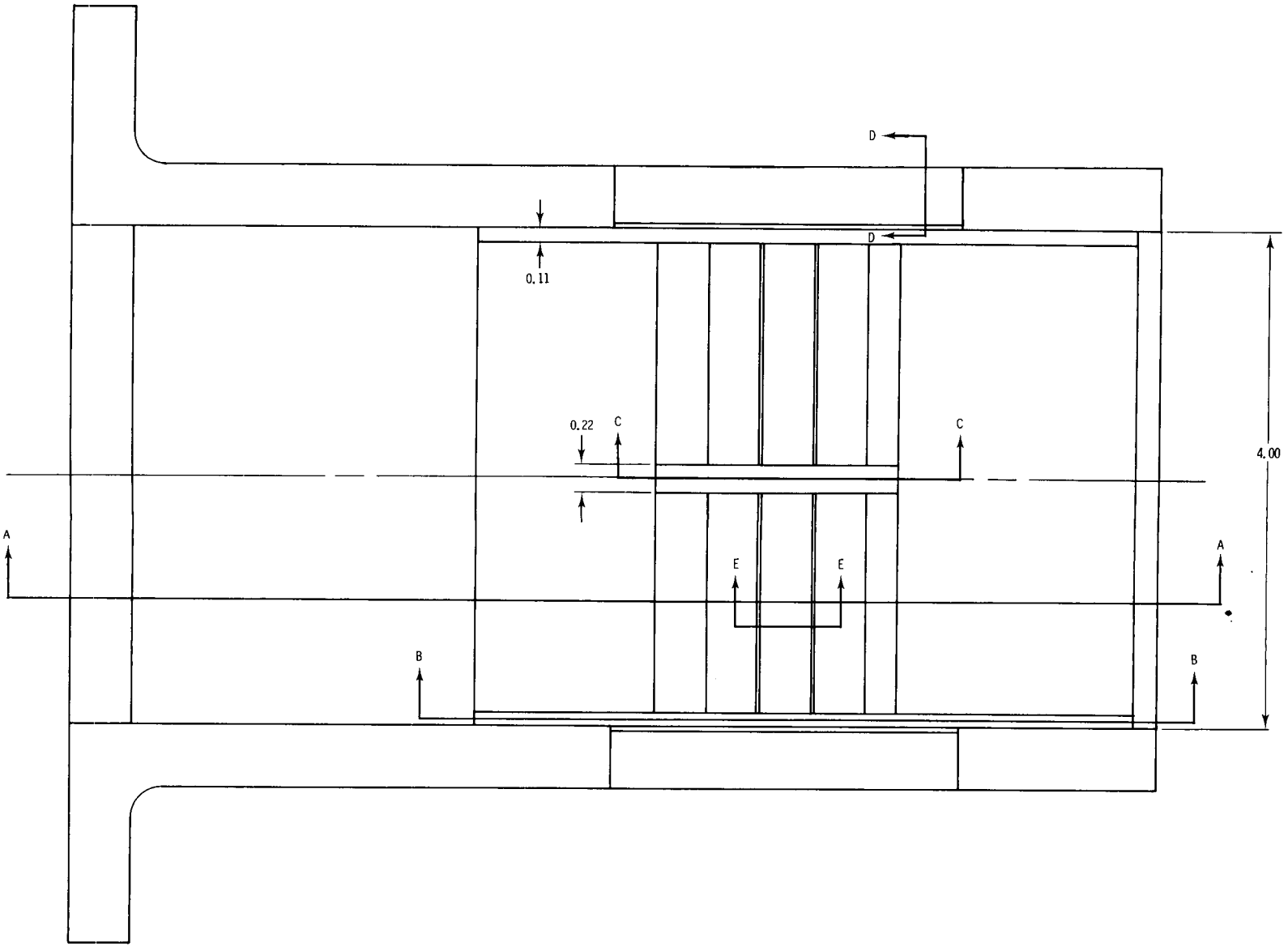

(a) Top view.

Figure 3. Sketches of thrust reverser test hardware showing important geometry. All dimensions are in inches unless otherwise noted.

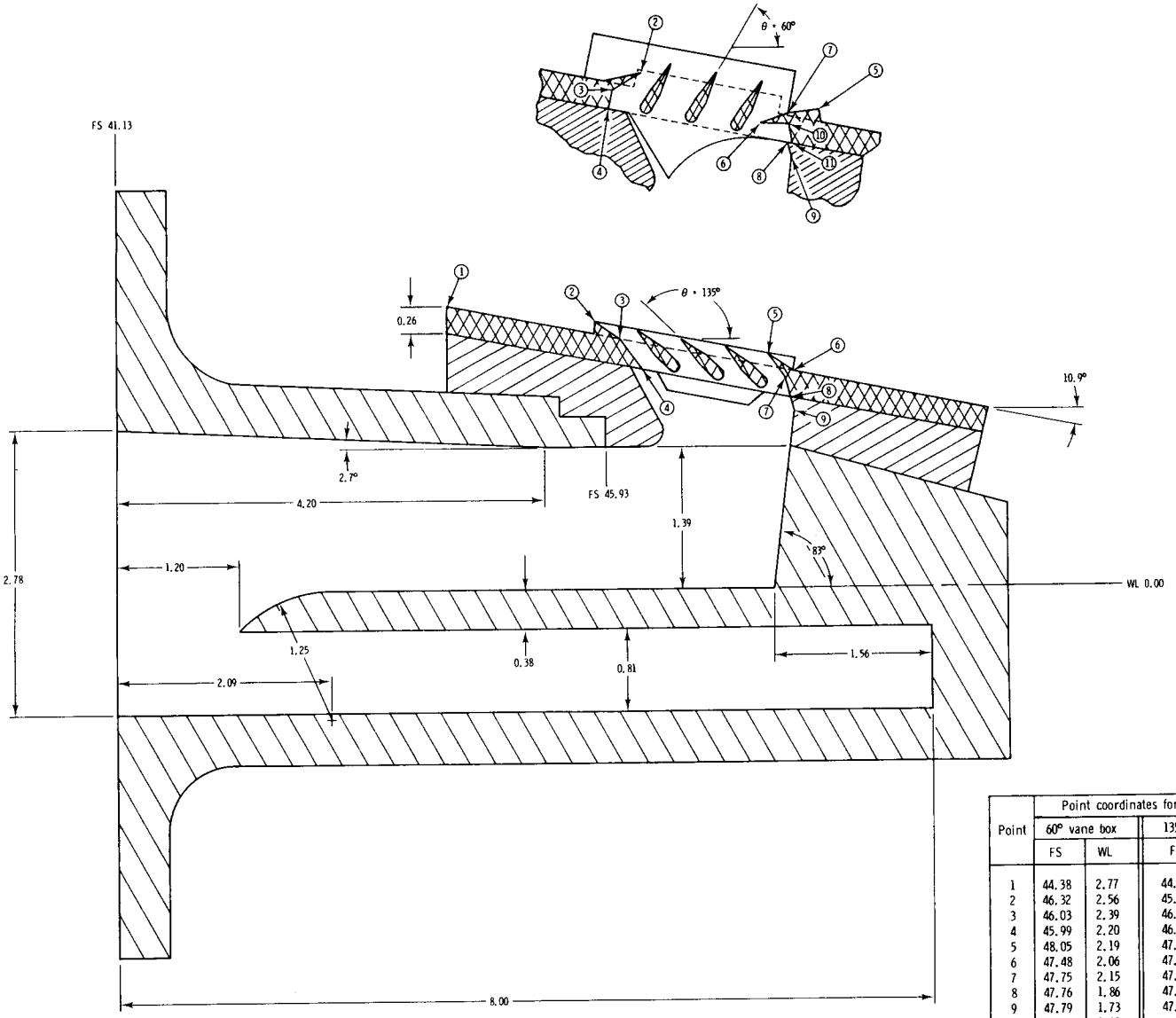

Point	Point coordinates for –			
	60° vane box		135° vane box	
	FS	WL	FS	WL
1	44.38	2.77	44.38	2.77
2	46.32	2.56	45.79	2.65
3	46.03	2.39	46.08	2.44
4	45.99	2.20	46.30	2.14
5	48.05	2.19	47.49	2.32
6	47.48	2.06	47.77	2.11
7	47.75	2.15	47.70	2.04
8	47.76	1.86	47.76	1.86
9	47.79	1.73	47.79	1.73
10	47.76	2.05	-	-
11	47.79	1.85	-	-

(b) Section A-A.

Figure 3. Continued.

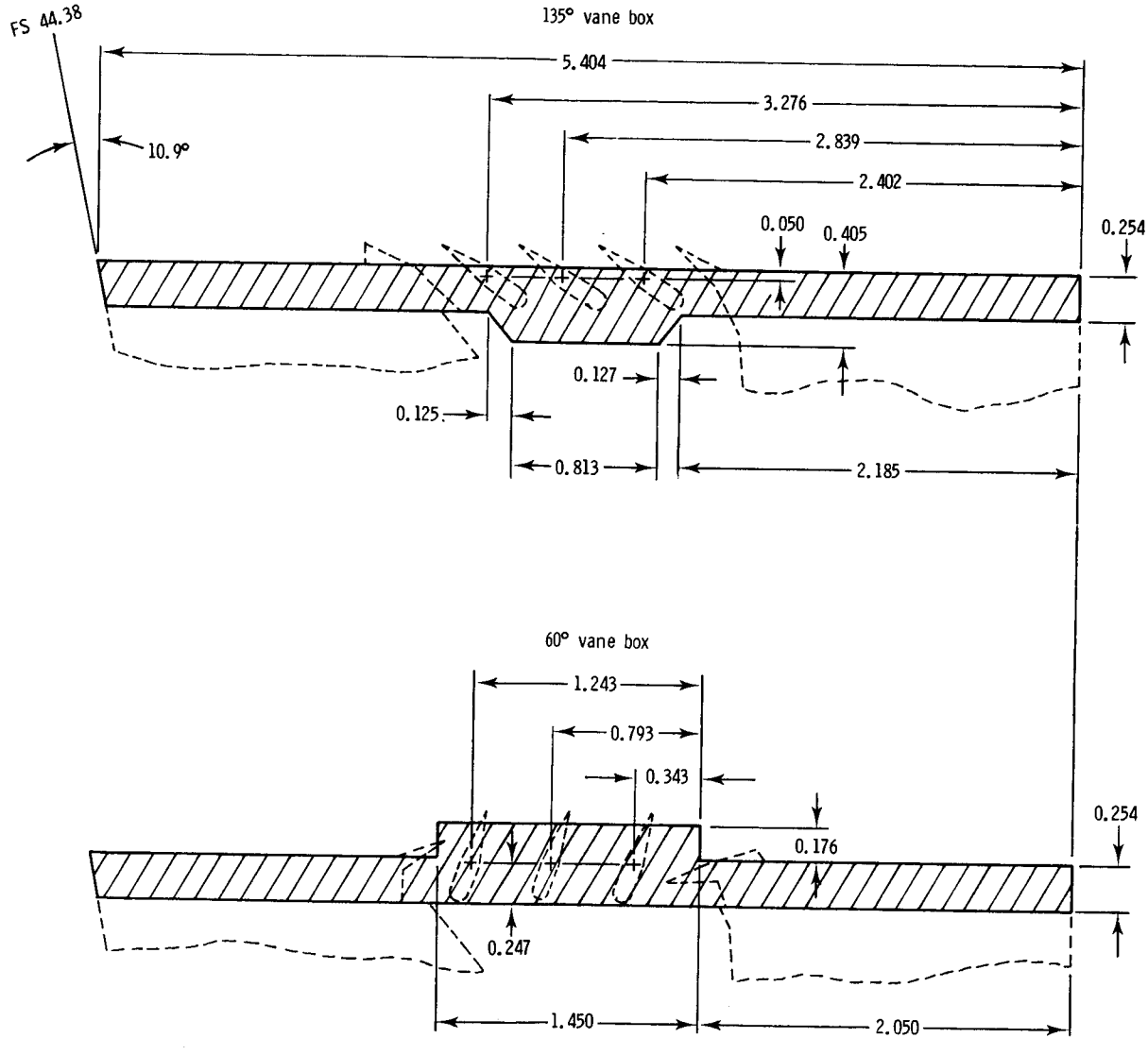

(c) Section B-B (vane box sidewall).

Figure 3. Continued.

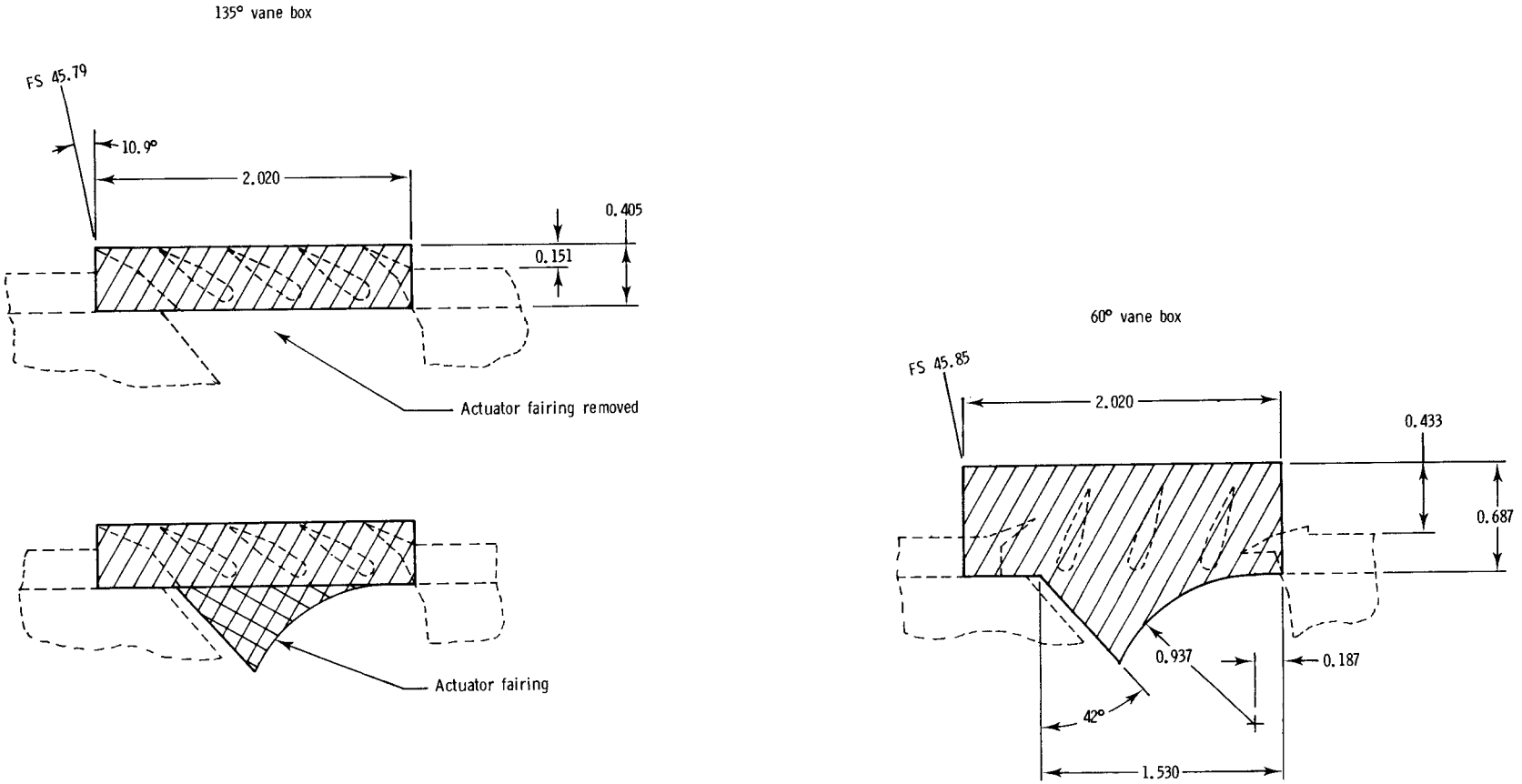

(d) Section C-C (vane box center wall).

Figure 3. Continued.

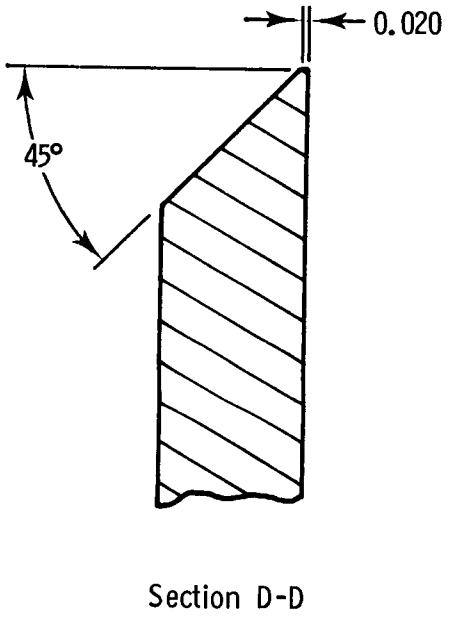

Section D-D

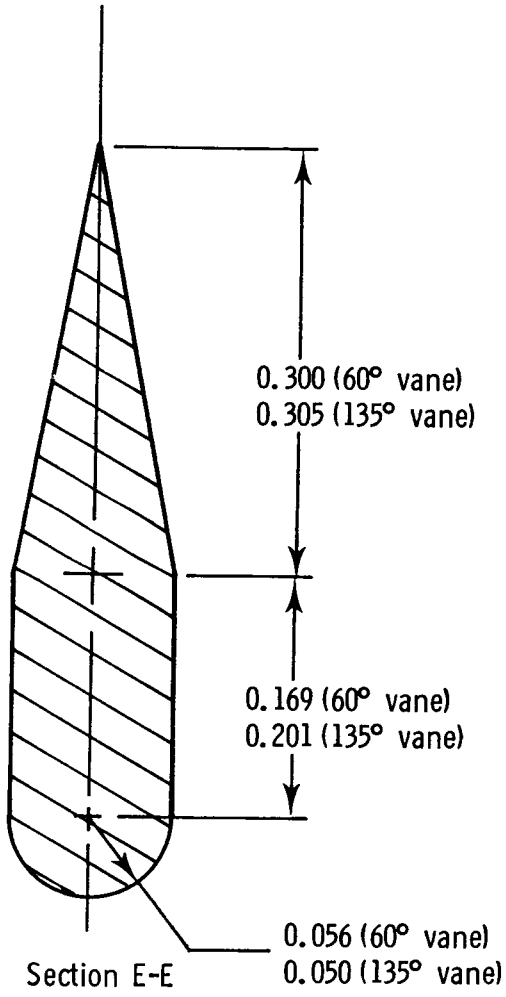

Section E-E

Note: Section E-E is drawn at 5 times the scale of Section D-D.

(e) Section D-D and section E-E.

Figure 3. Concluded.

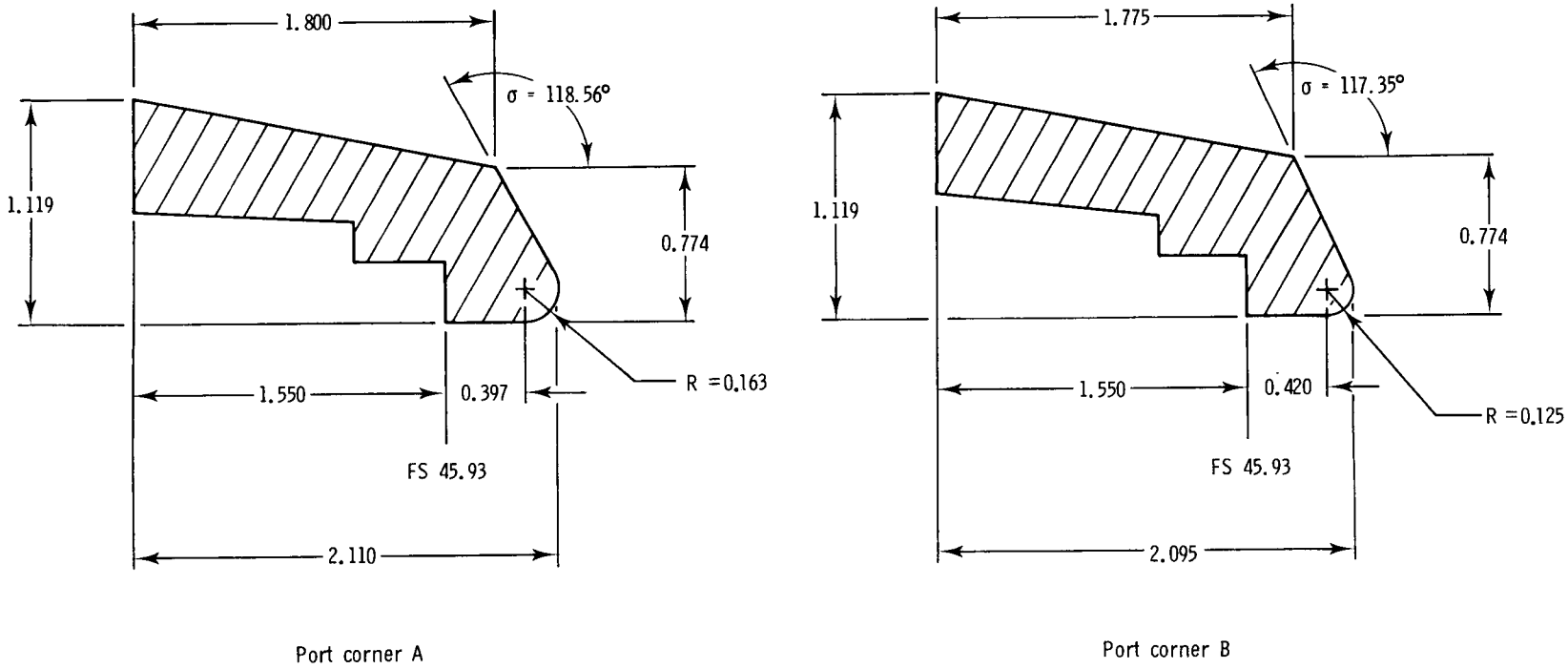

(a) Port corners A and B.

Figure 4. Sketches of port corner configurations showing important dimensions. All dimensions are in inches unless otherwise noted.

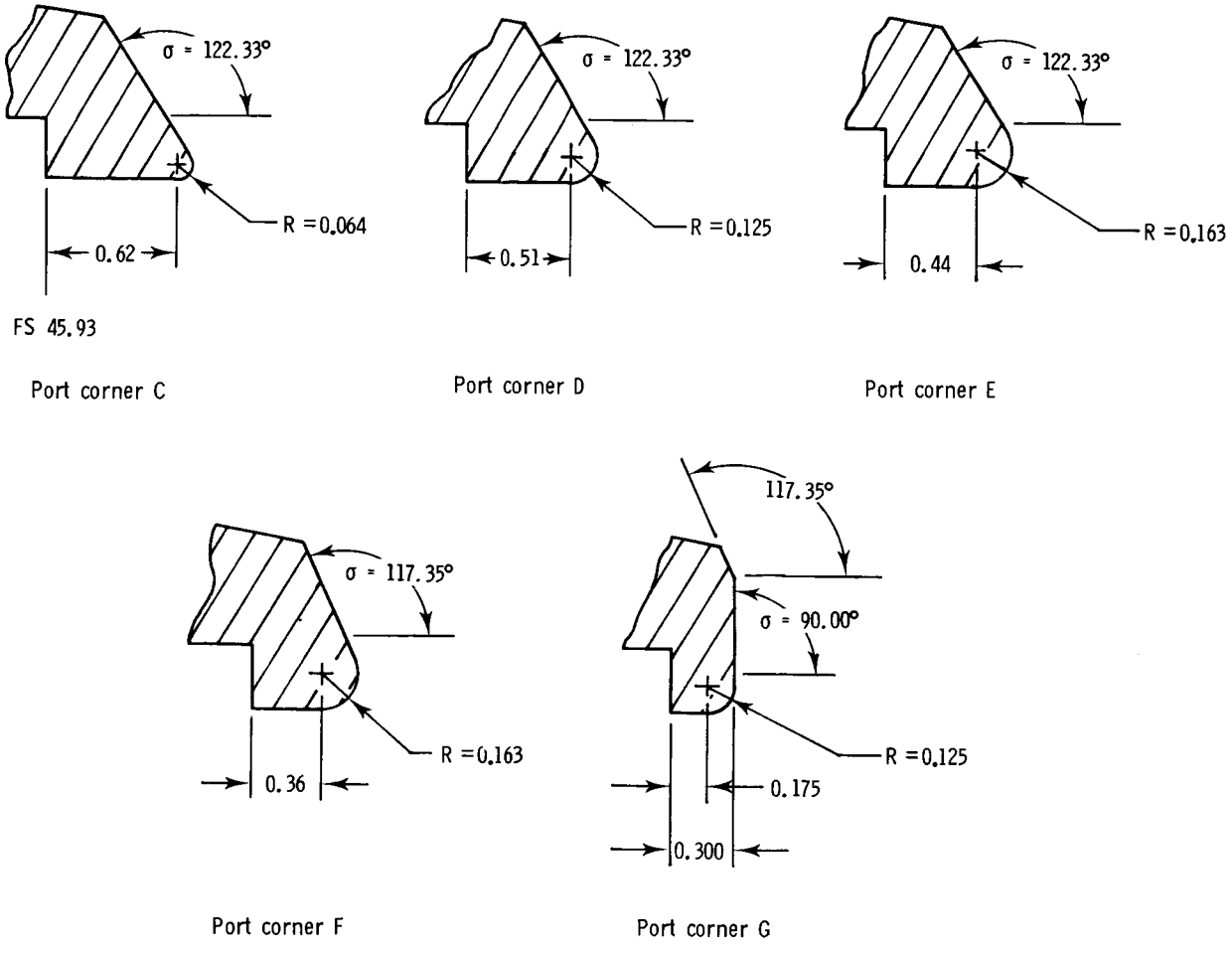

(b) Port corners C to G.

Figure 4. Continued.

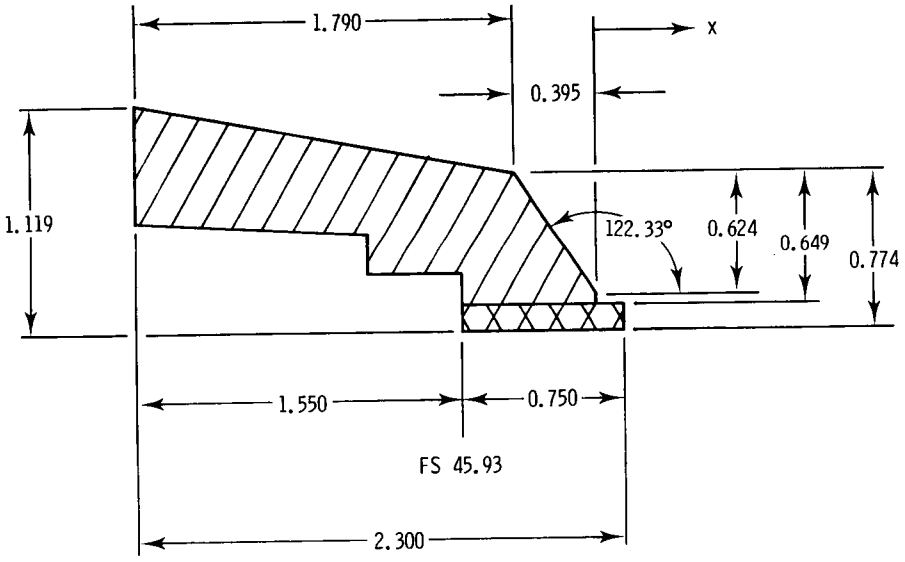

Port corner H

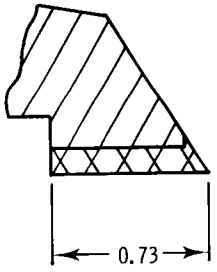

Port corner M

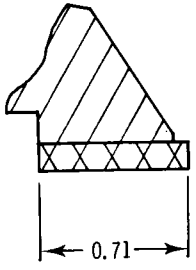

Port corner I

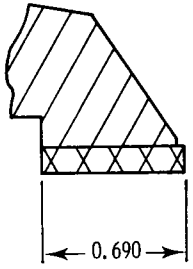

Port corner J

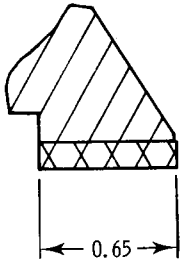

Port corner K

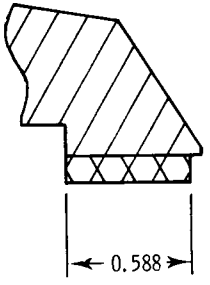

Port corner L

(c) Port corners H to M.

Figure 4. Concluded.

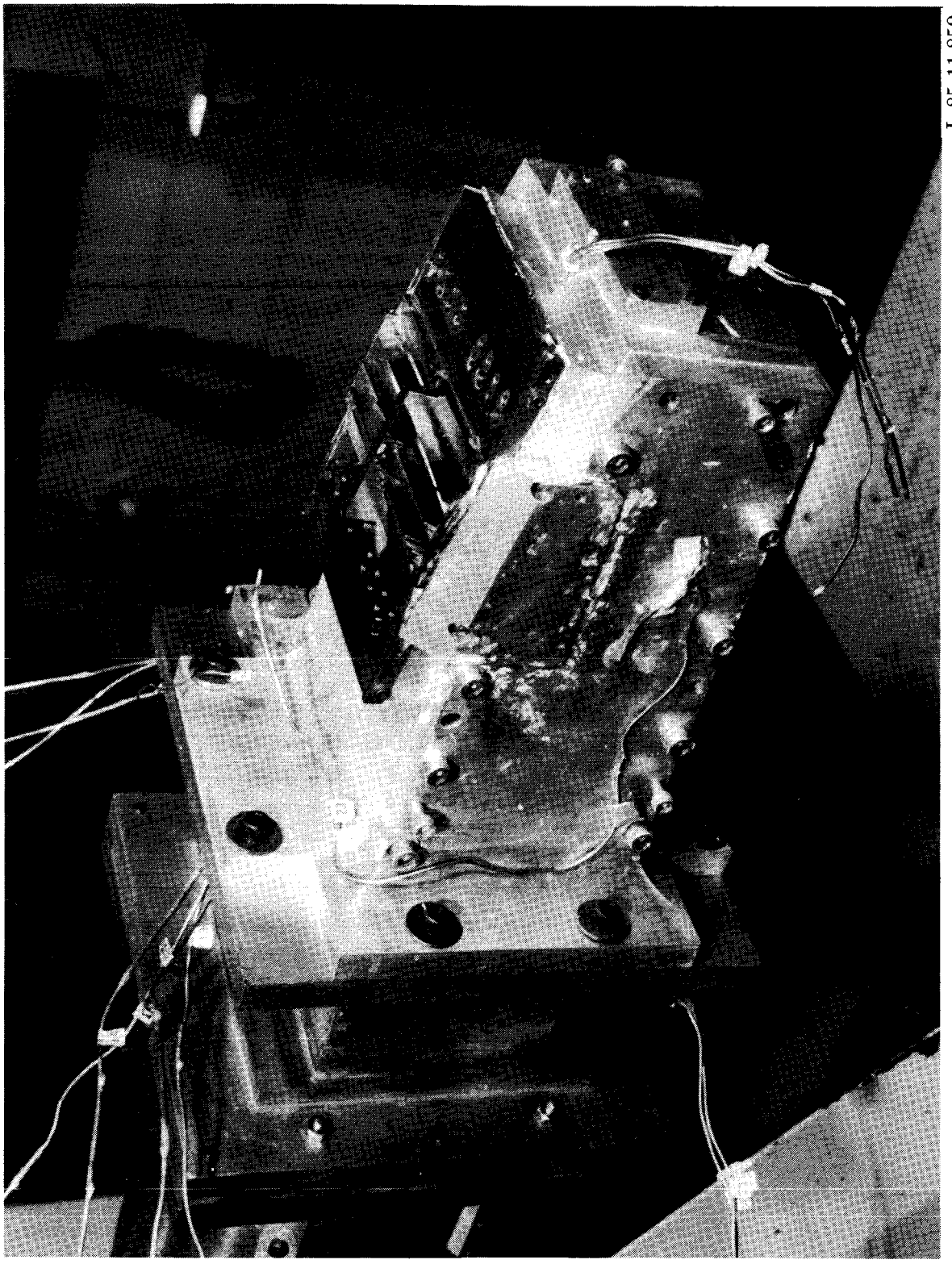

L-85-11,850

(a) 60° vane configuration.

Figure 5. Reverser port configurations.

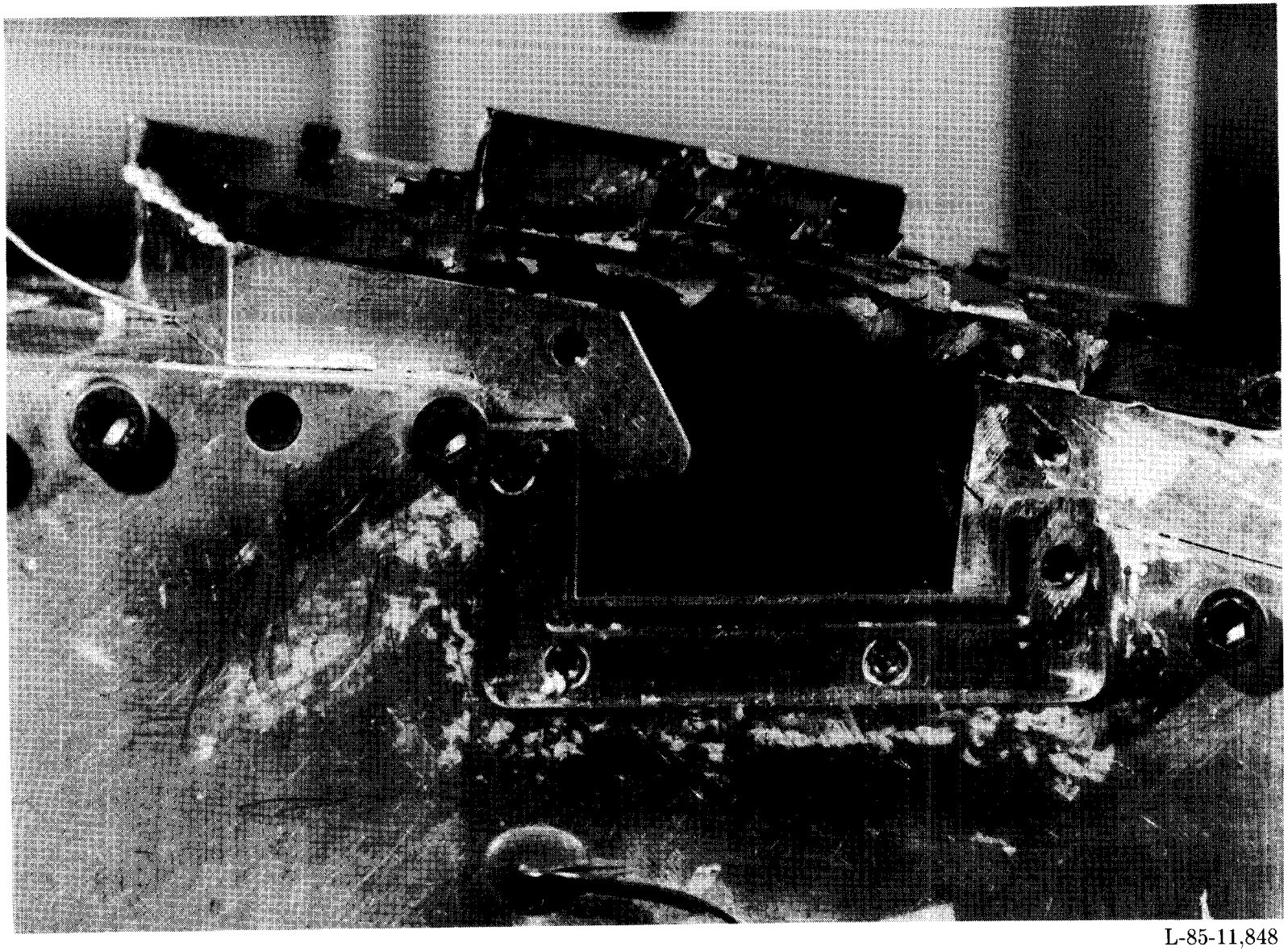

L-85-11,848

(b) Configuration 60°/B (port sidewall removed).

Figure 5. Continued.

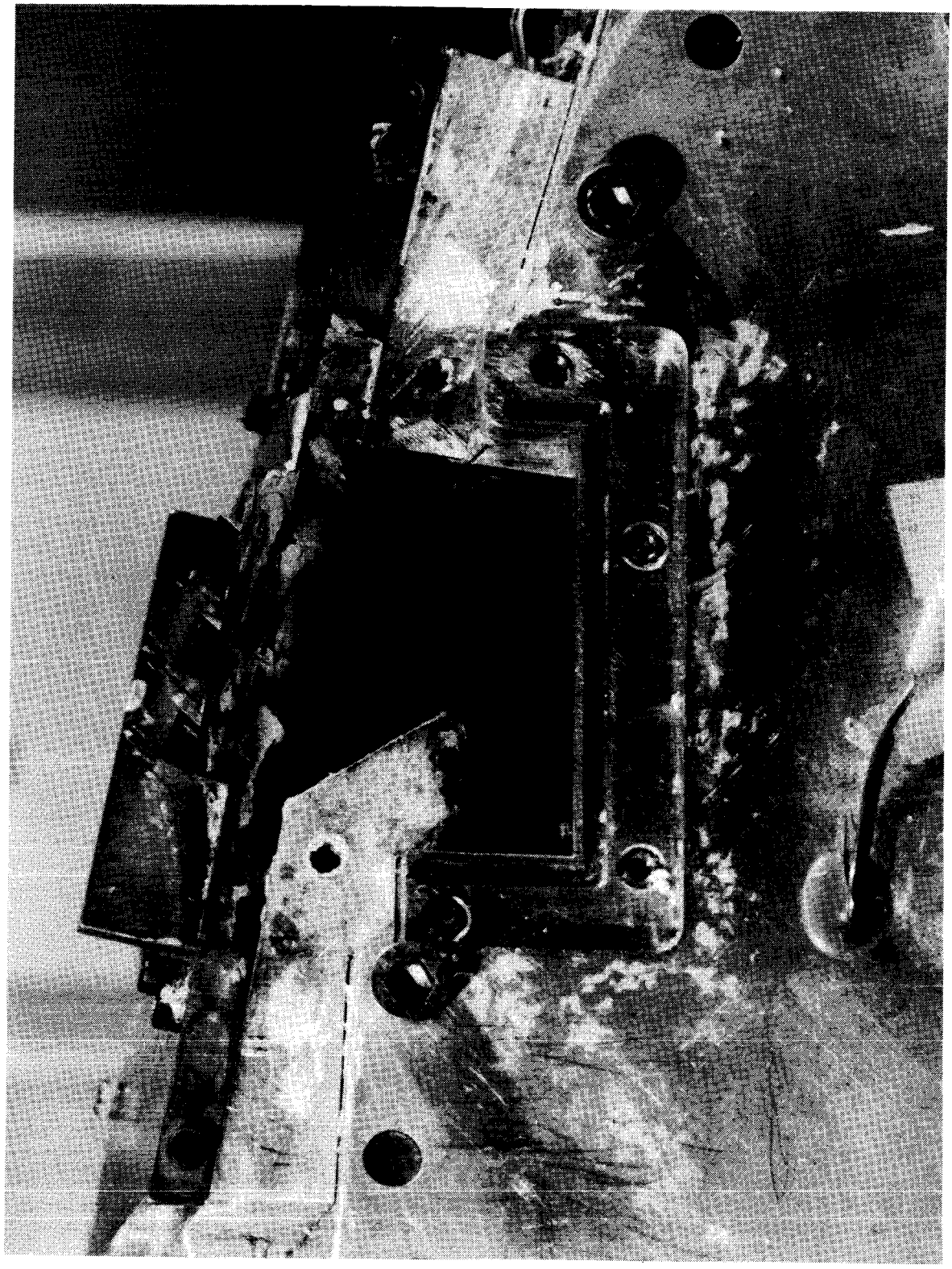

L-85-11,849

(c) Configuration 60°/M (port sidewall removed).

Figure 5. Concluded.

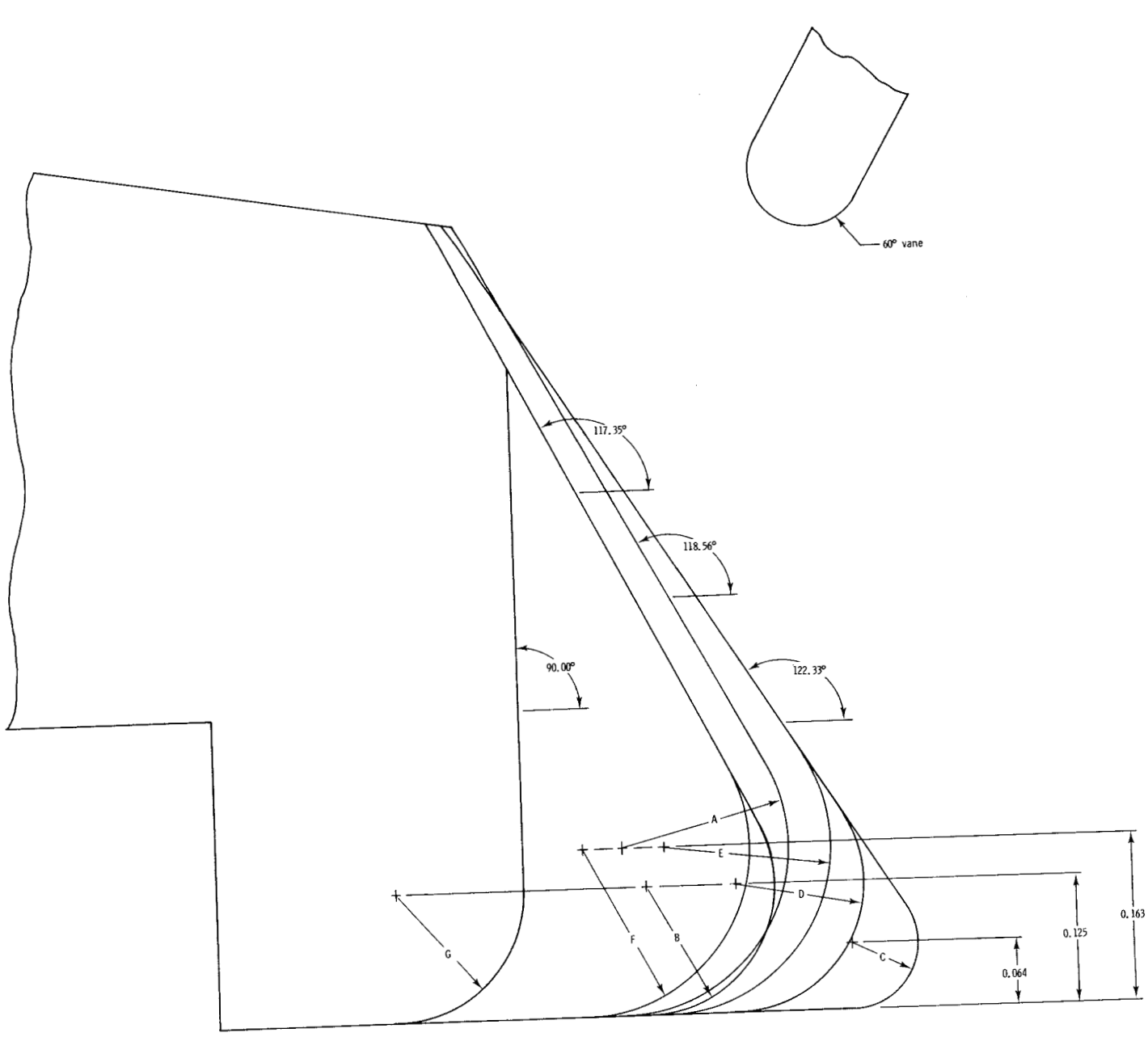

Figure 6. Sketch showing comparison of geometry for port corners A through G.

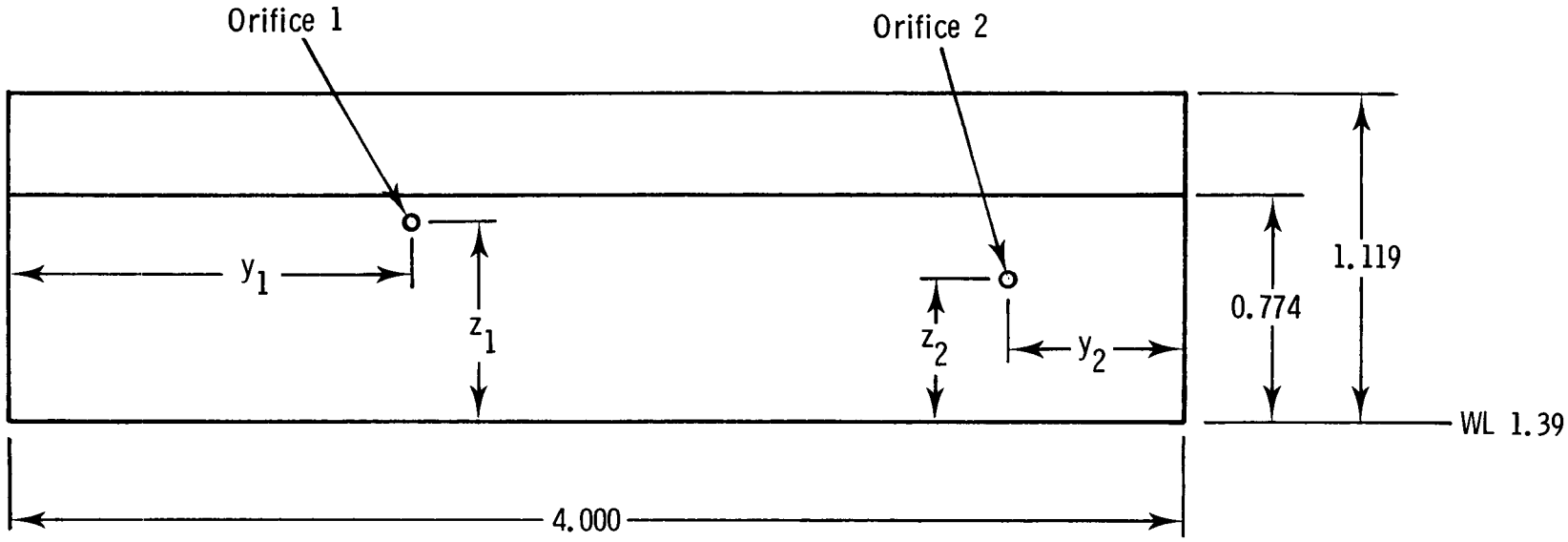

View of port corner (see fig. 4) face looking upstream

Port corner	y_1, in.	z_1, in.	y_2, in.	z_2, in.
A and B	-	-	-	-
C-E and H-M	1.37	0.68	0.60	0.49
F and G	1.35	0.65	0.81	0.40

Figure 7. Sketch showing location of pressure orifices on port corners.

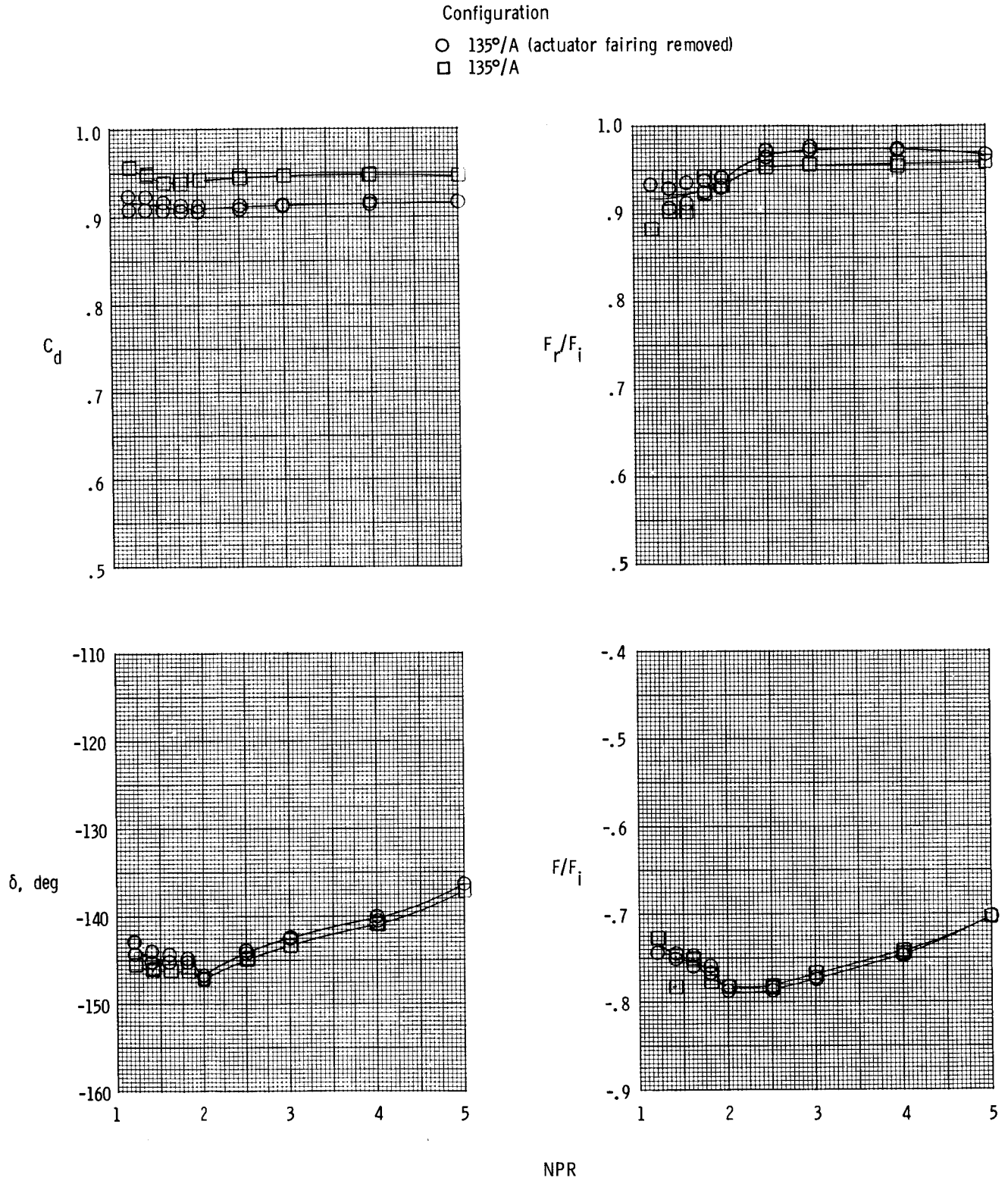

(a) 135° vane box.

Figure 8. Variation of static performance with nozzle pressure ratio for reverser having port corner with $\sigma = 118.56°$.

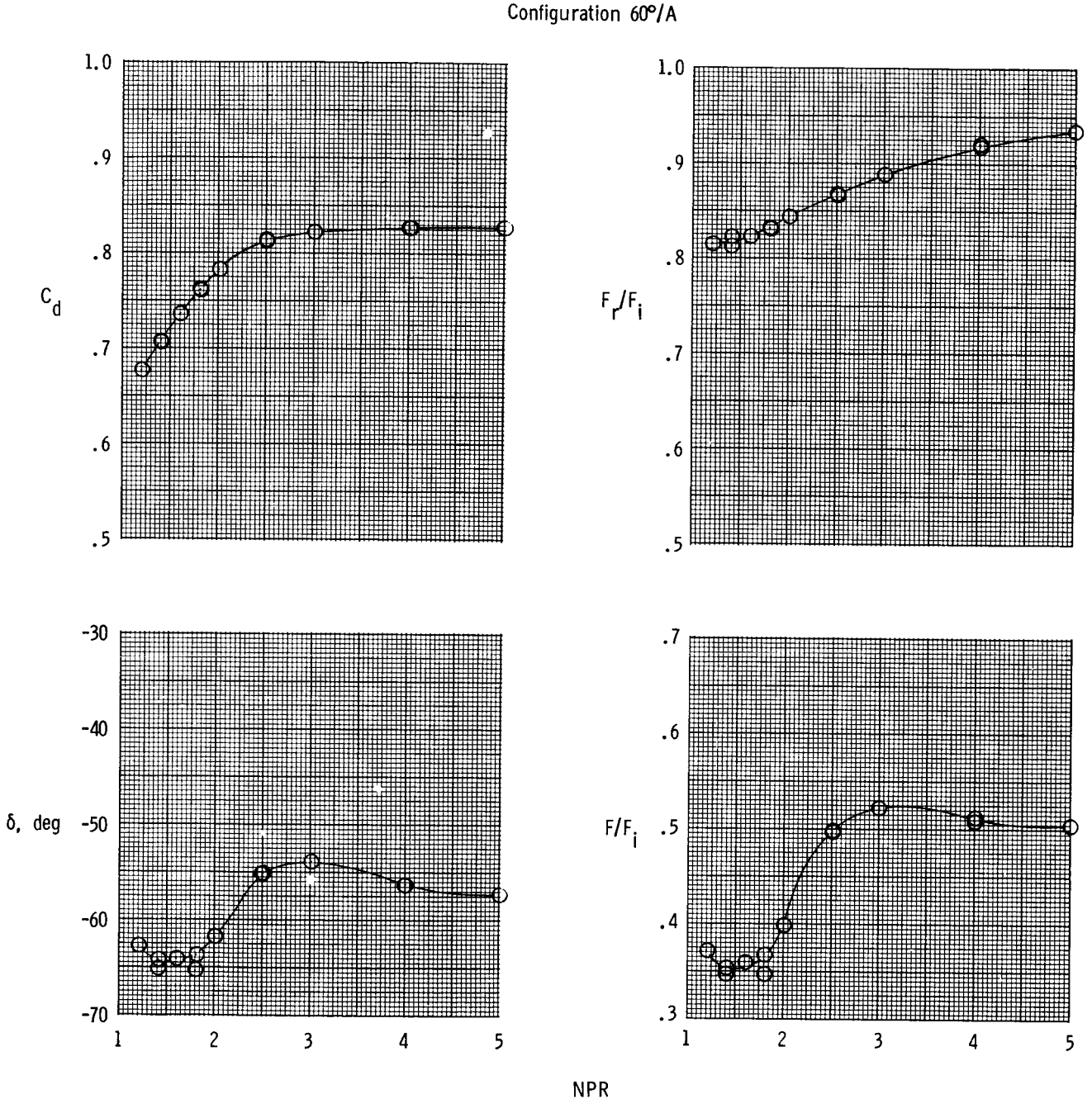

(b) 60° vane box.

Figure 8. Concluded.

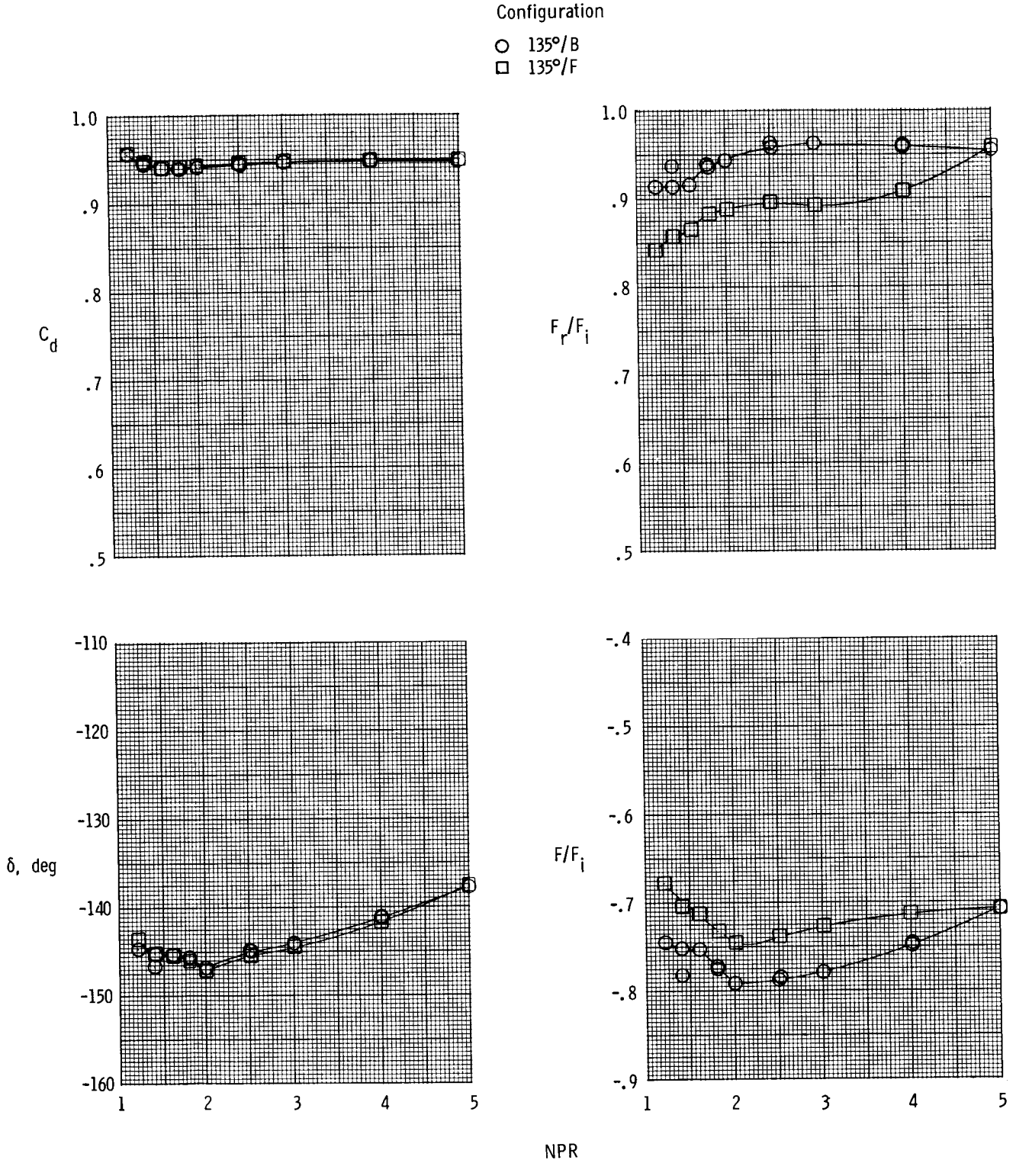

(a) 135° vane box.

Figure 9. Variation of static performance with nozzle pressure ratio for reverser having port corners with $\sigma = 117.35°$.

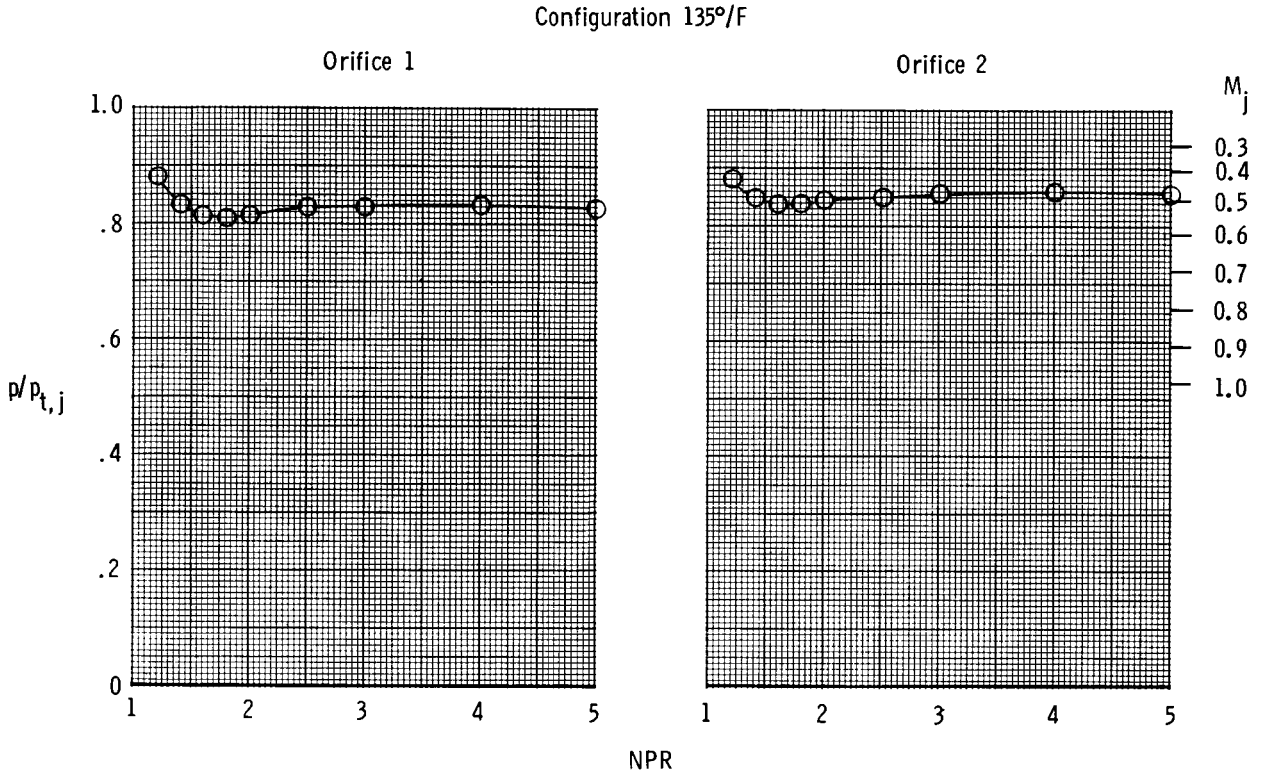

(a) Concluded.

Figure 9. Continued.

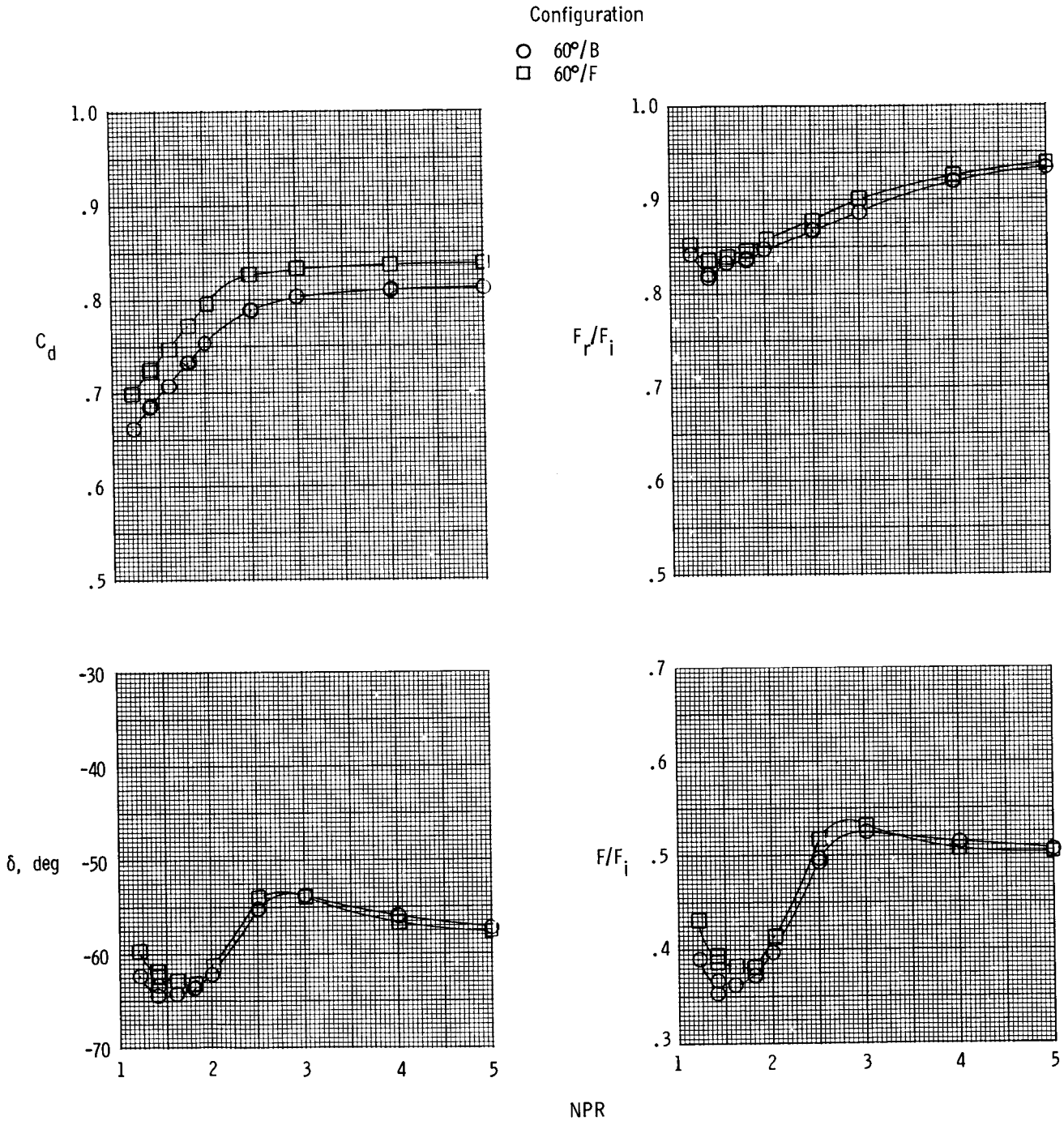

(b) 60° vane box.

Figure 9. Continued.

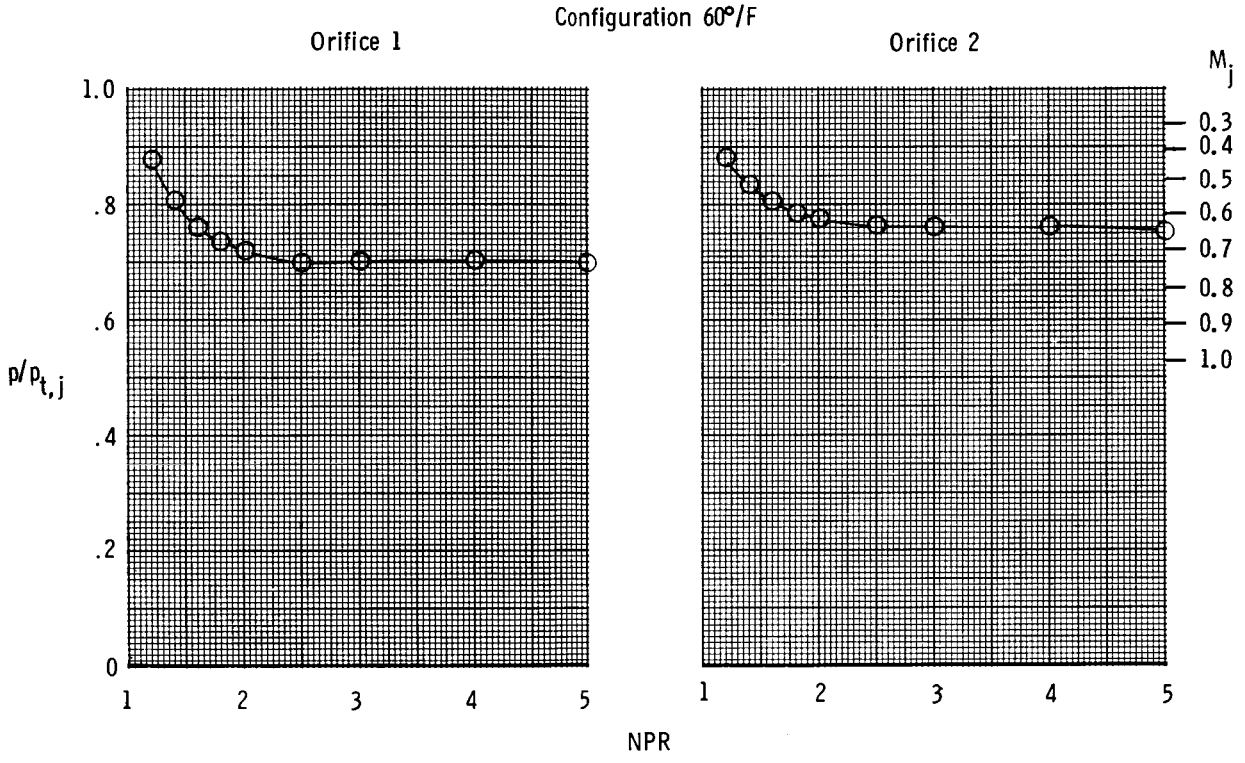

(b) Concluded.

Figure 9. Concluded.

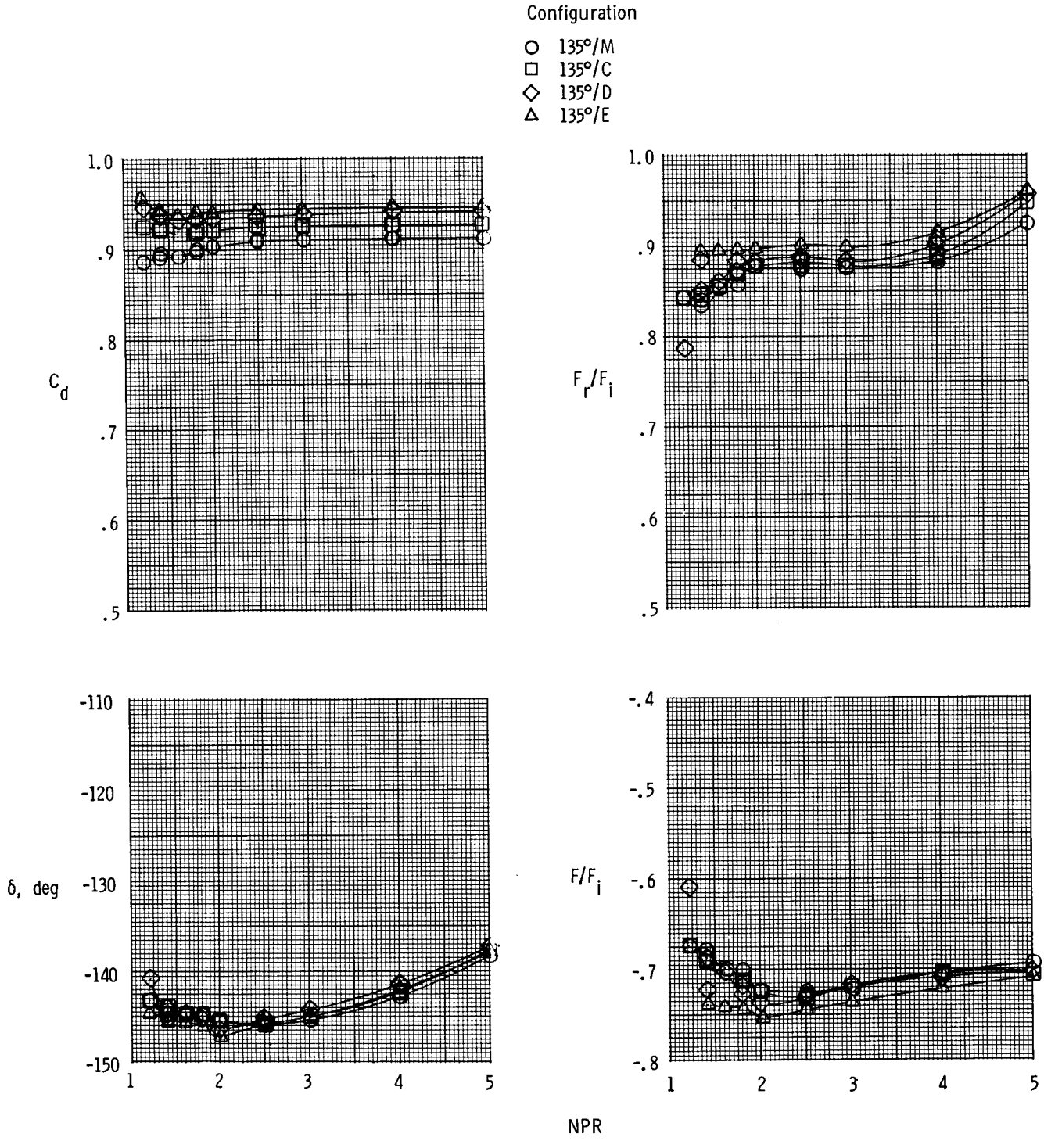

(a) 135° vane box.

Figure 10. Variation of static performance with nozzle pressure ratio for reverser having port corners with $\sigma = 122.33°$.

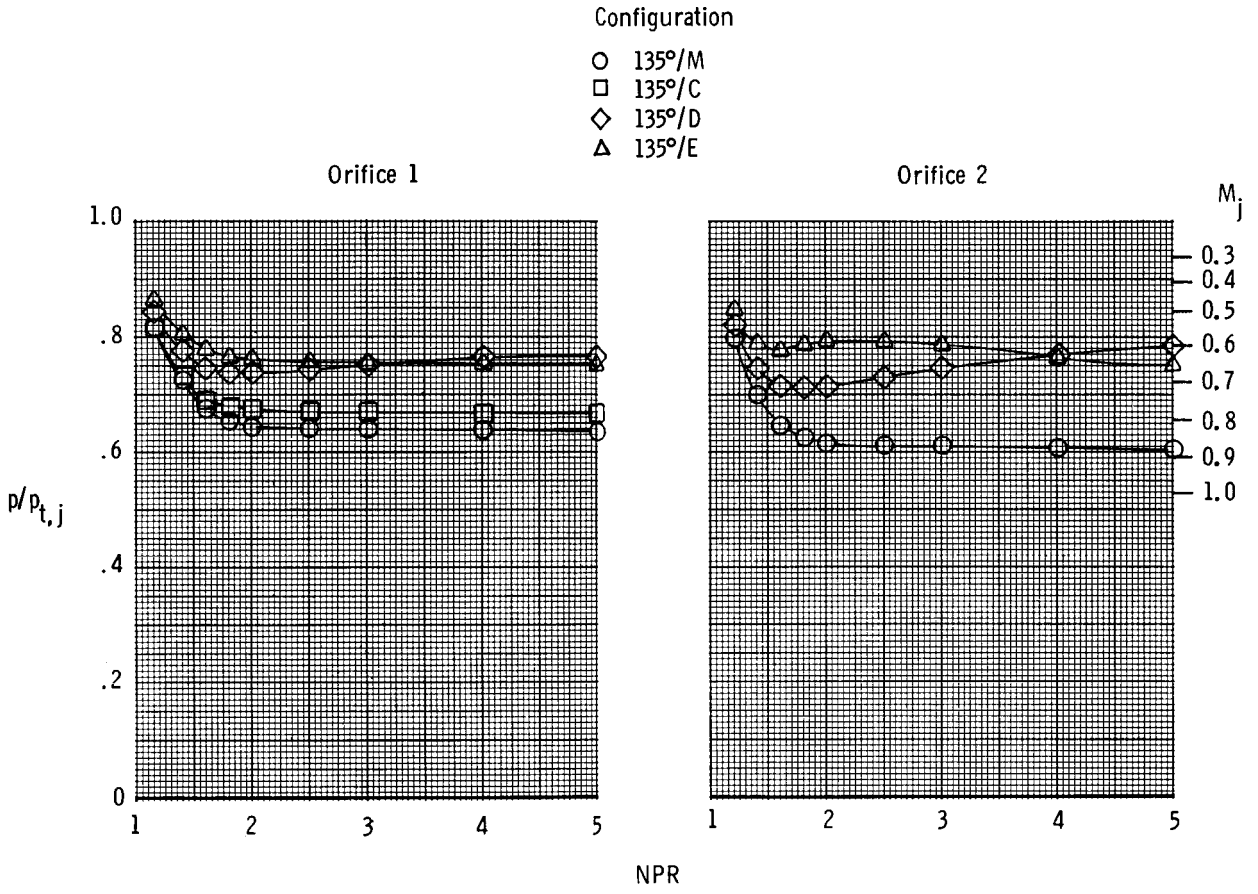

(a) Concluded.

Figure 10. Continued.

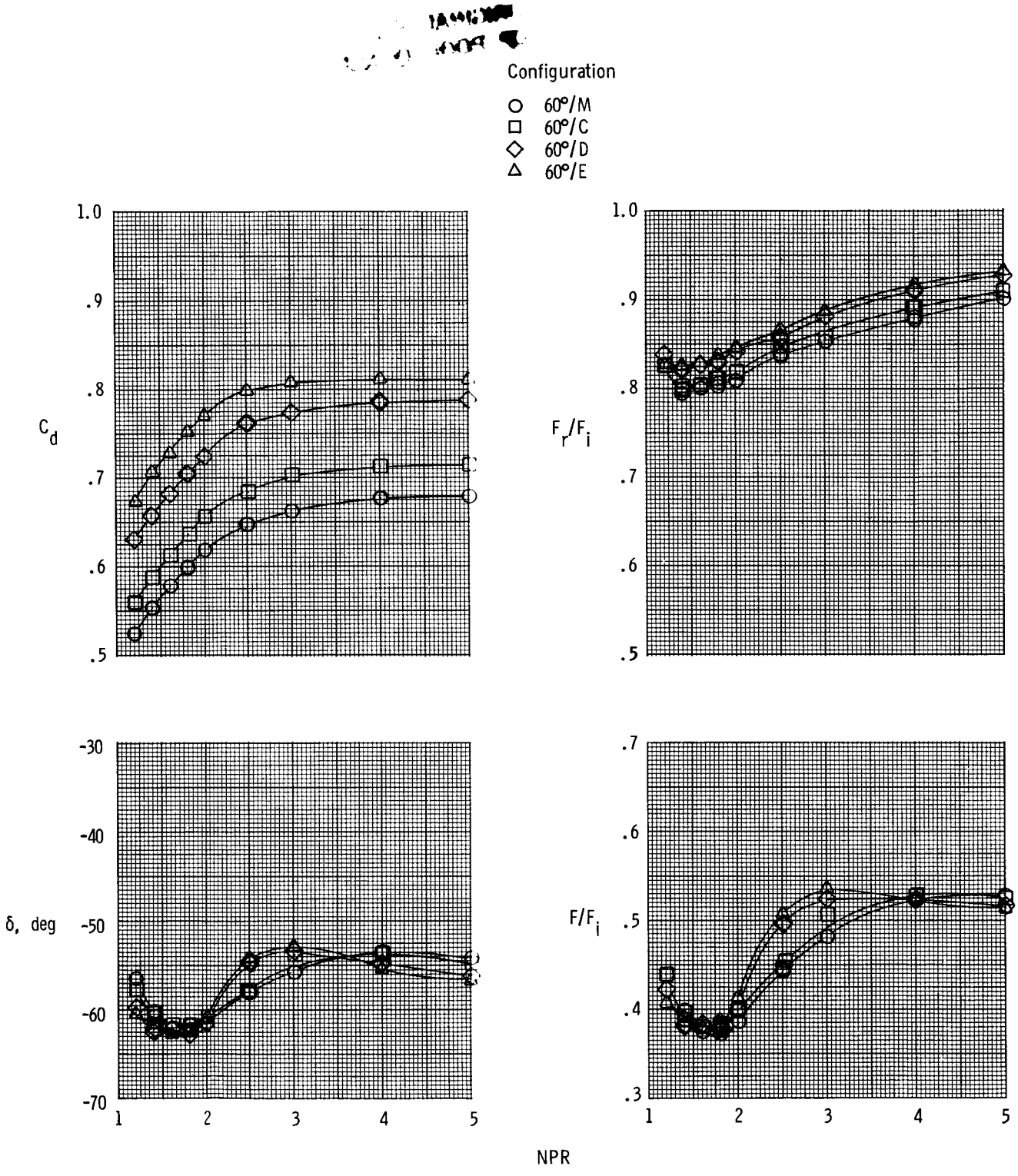

(b) 60° vane box.

Figure 10. Continued.

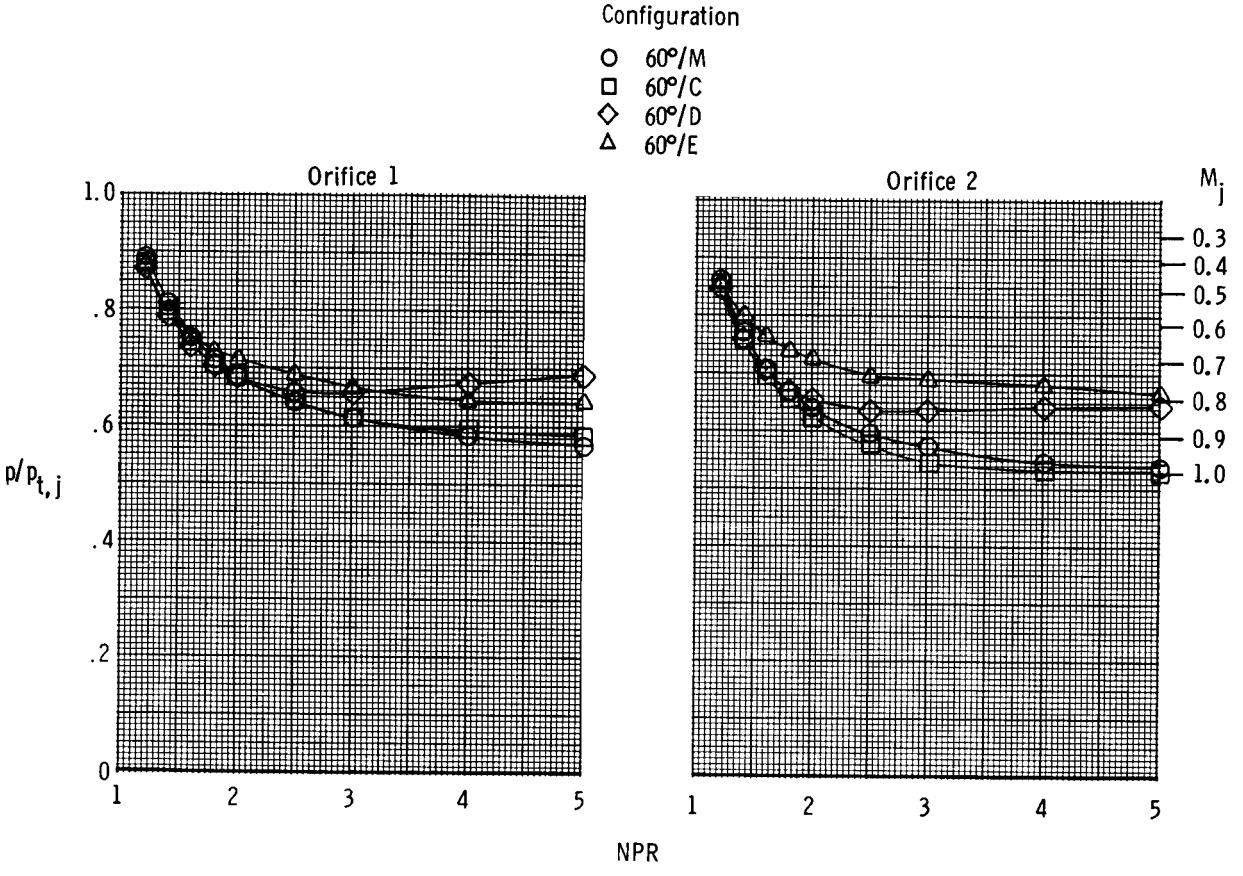

(b) Concluded.

Figure 10. Concluded.

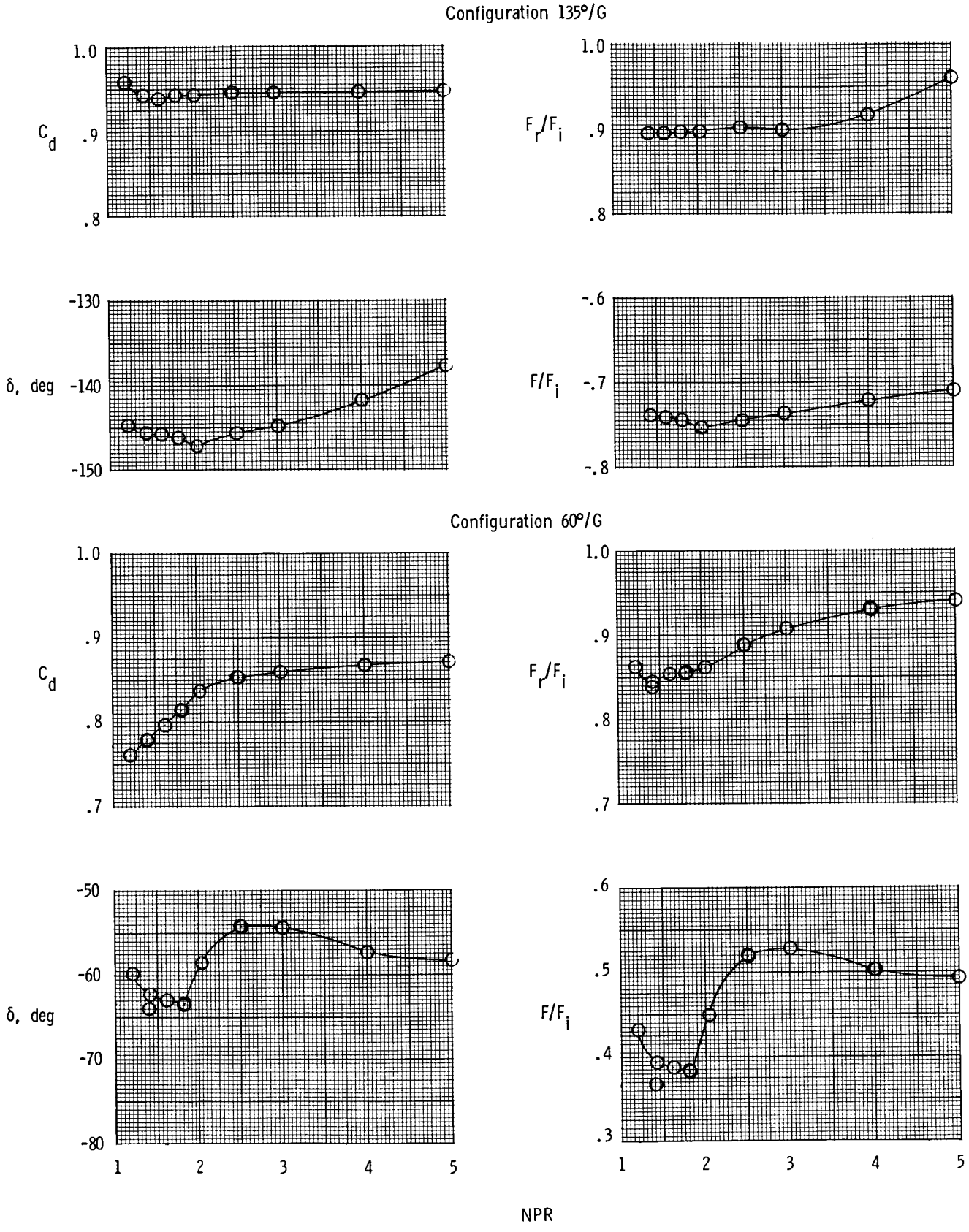

(a) Thrust and discharge coefficient performance.

Figure 11. Variation of static performance with nozzle pressure ratio for reverser having port corners with $\sigma = 90.00°$

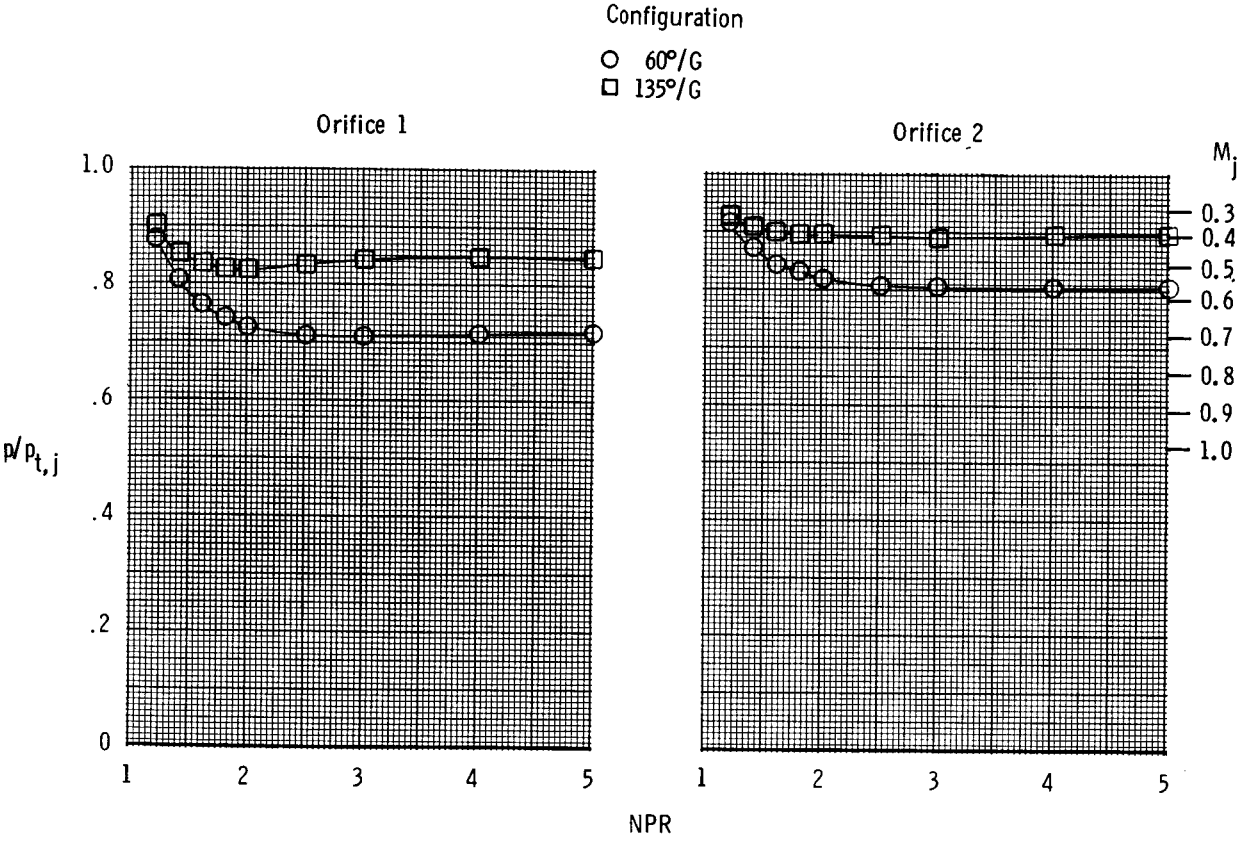

(b) Pressure ratios.

Figure 11. Concluded.

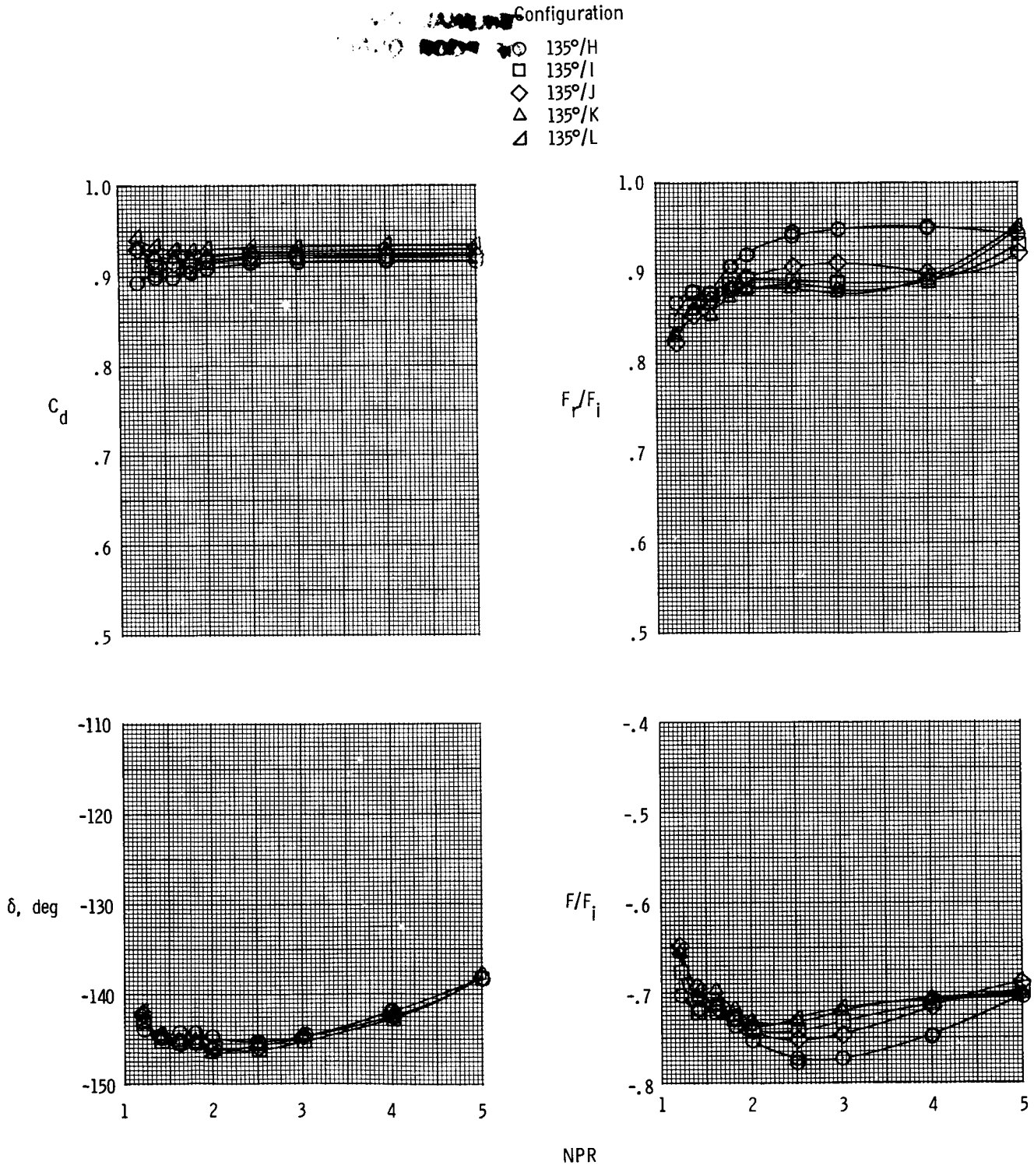

(a) 135° vane box.

Figure 12. Variation of static performance with nozzle pressure ratio for reverser having port corners with $\sigma = 122.33°$ and a simulated cooling liner.

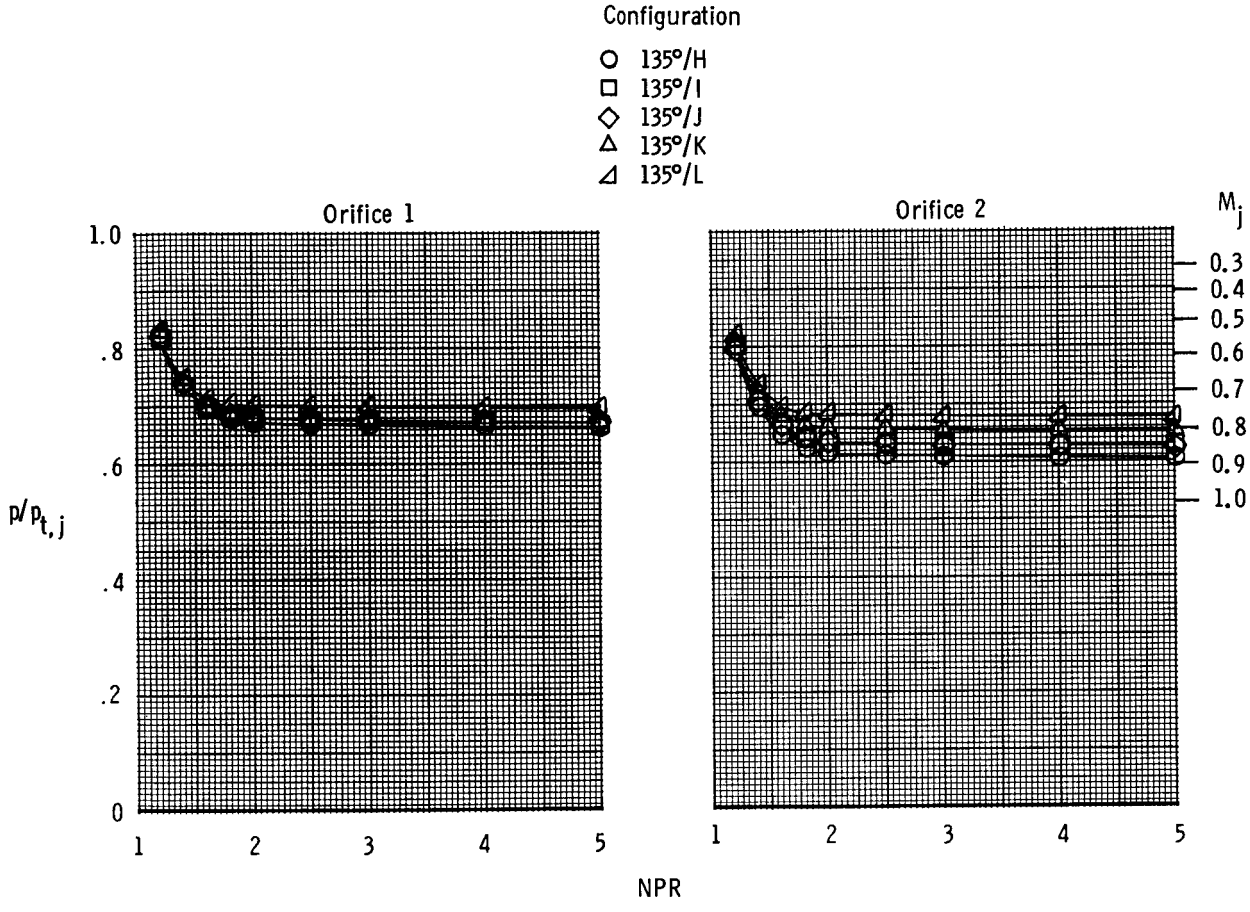

(a) Concluded.

Figure 12. Continued.

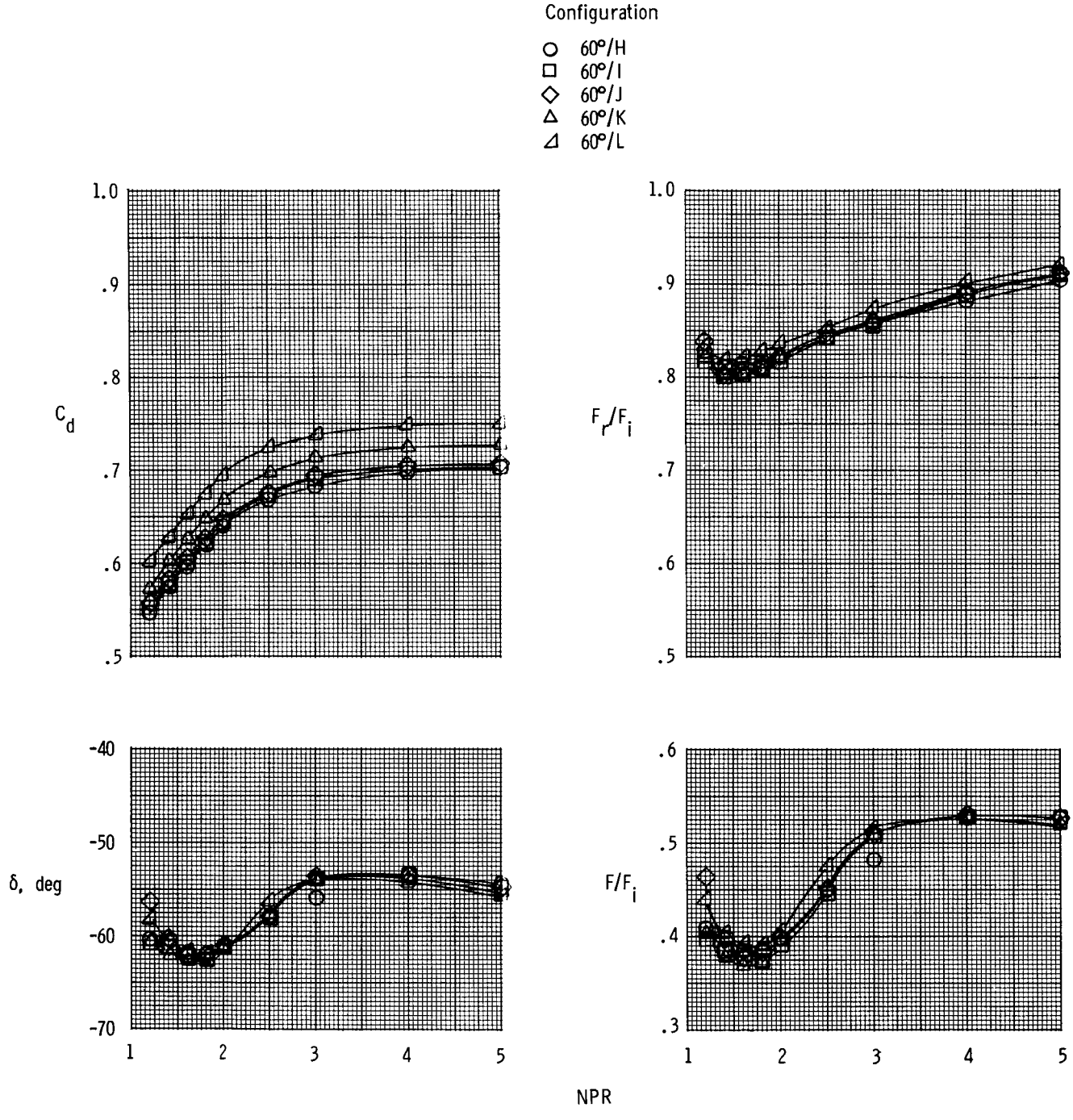

(b) 60° vane box.

Figure 12. Continued.

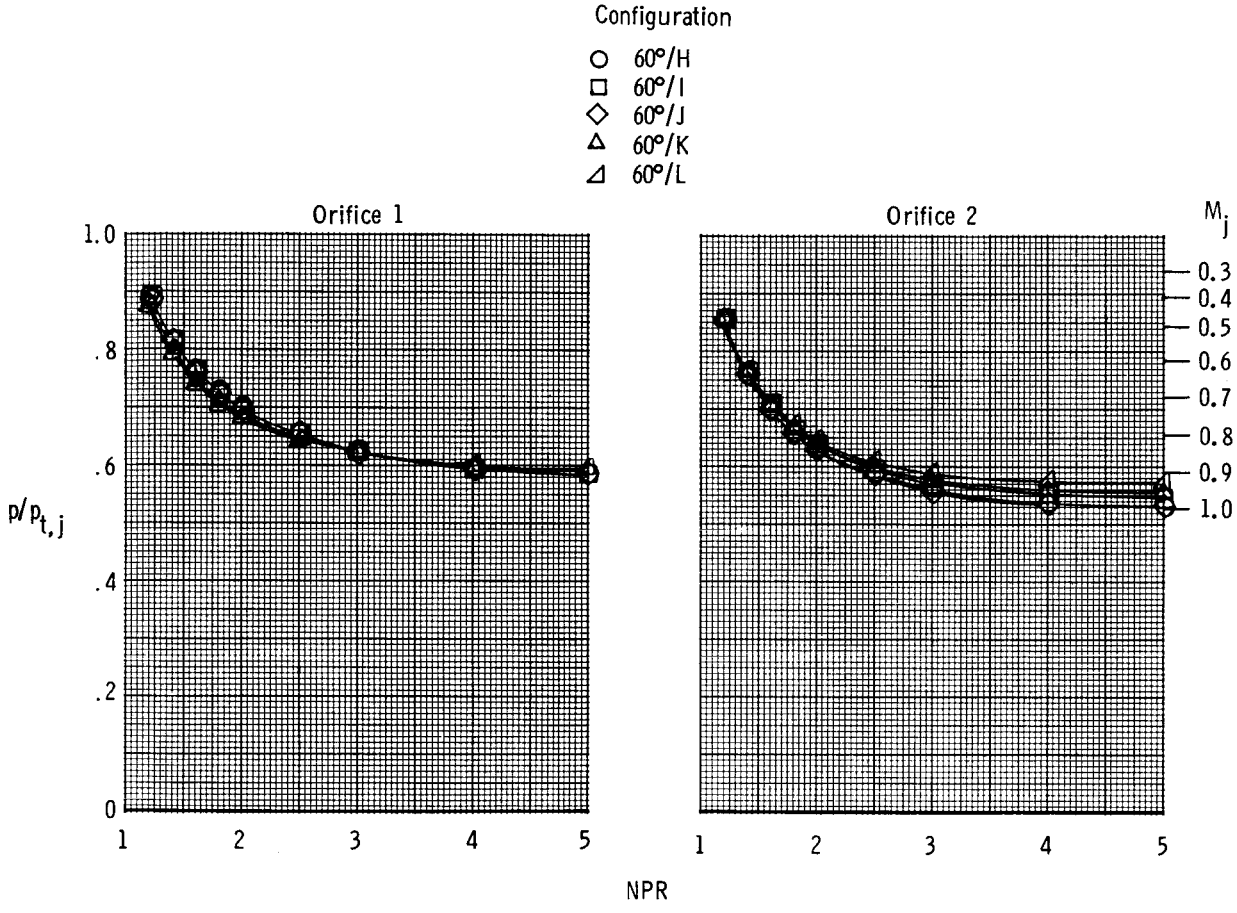

(b) Concluded.

Figure 12. Concluded.

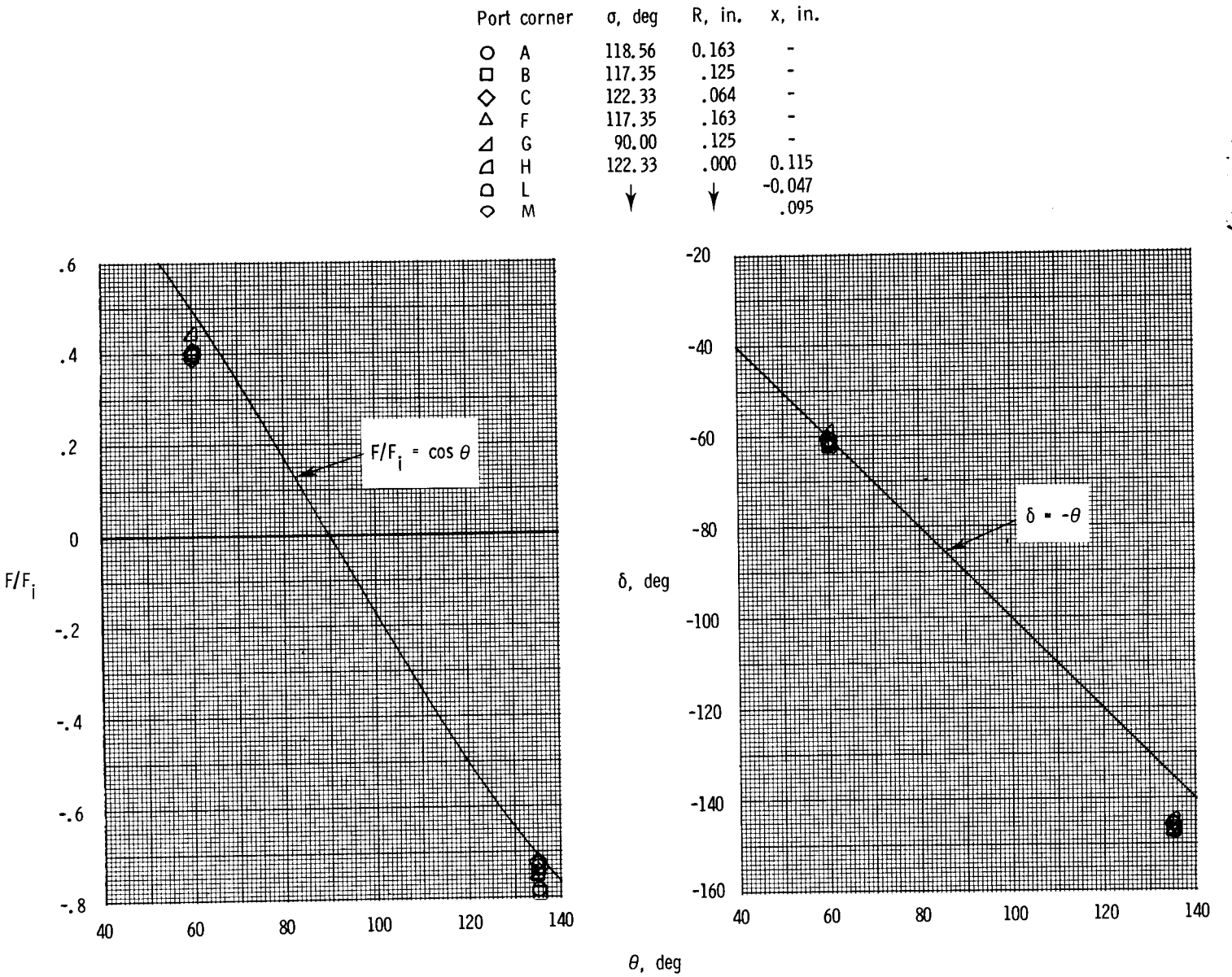

(a) NPR = 2.0.

Figure 13. Effect of reverser vane angle on thrust ratio and reverser efflux (thrust vector) angle.

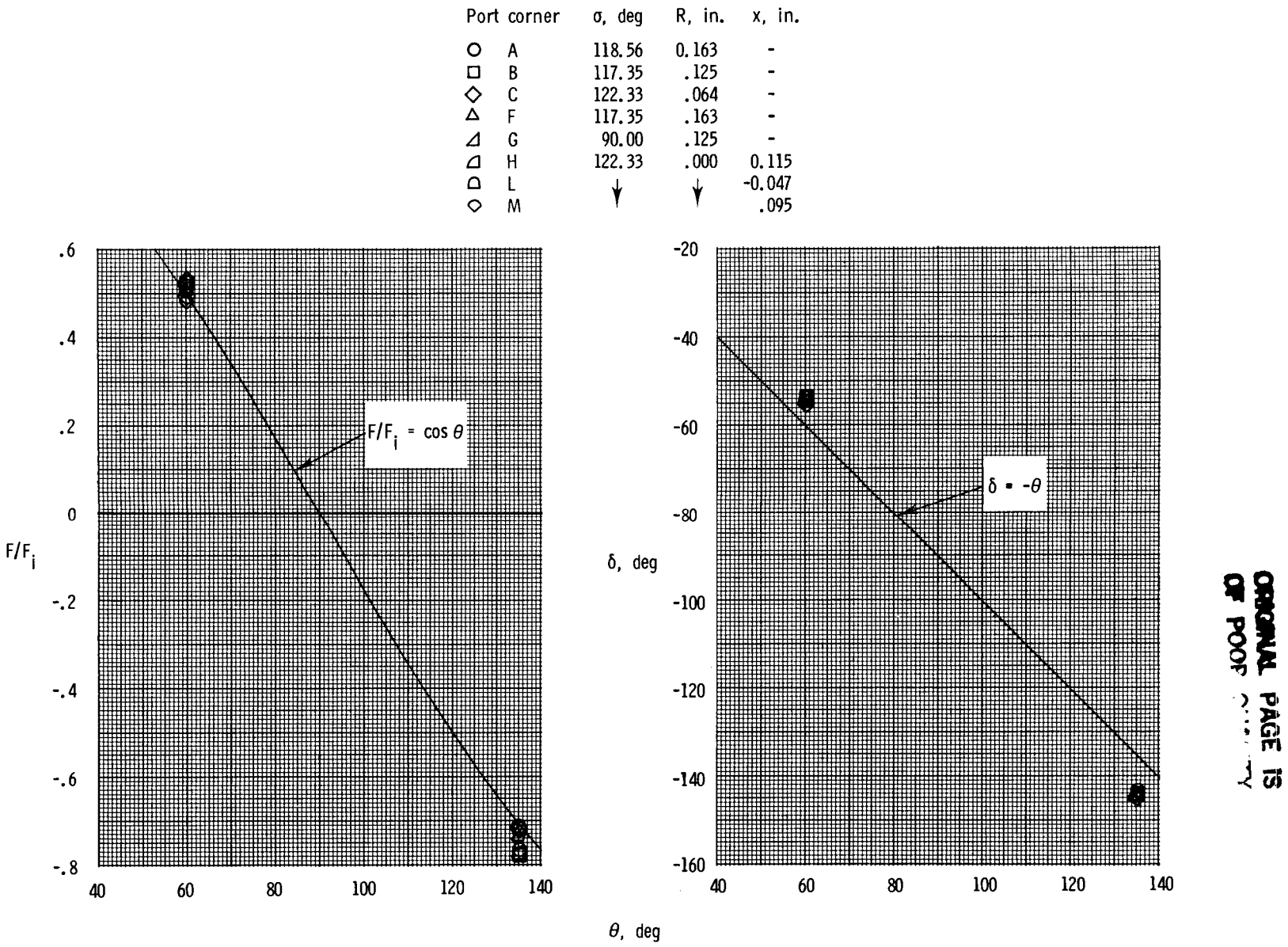

(b) NPR = 3.0.

Figure 13. Continued.

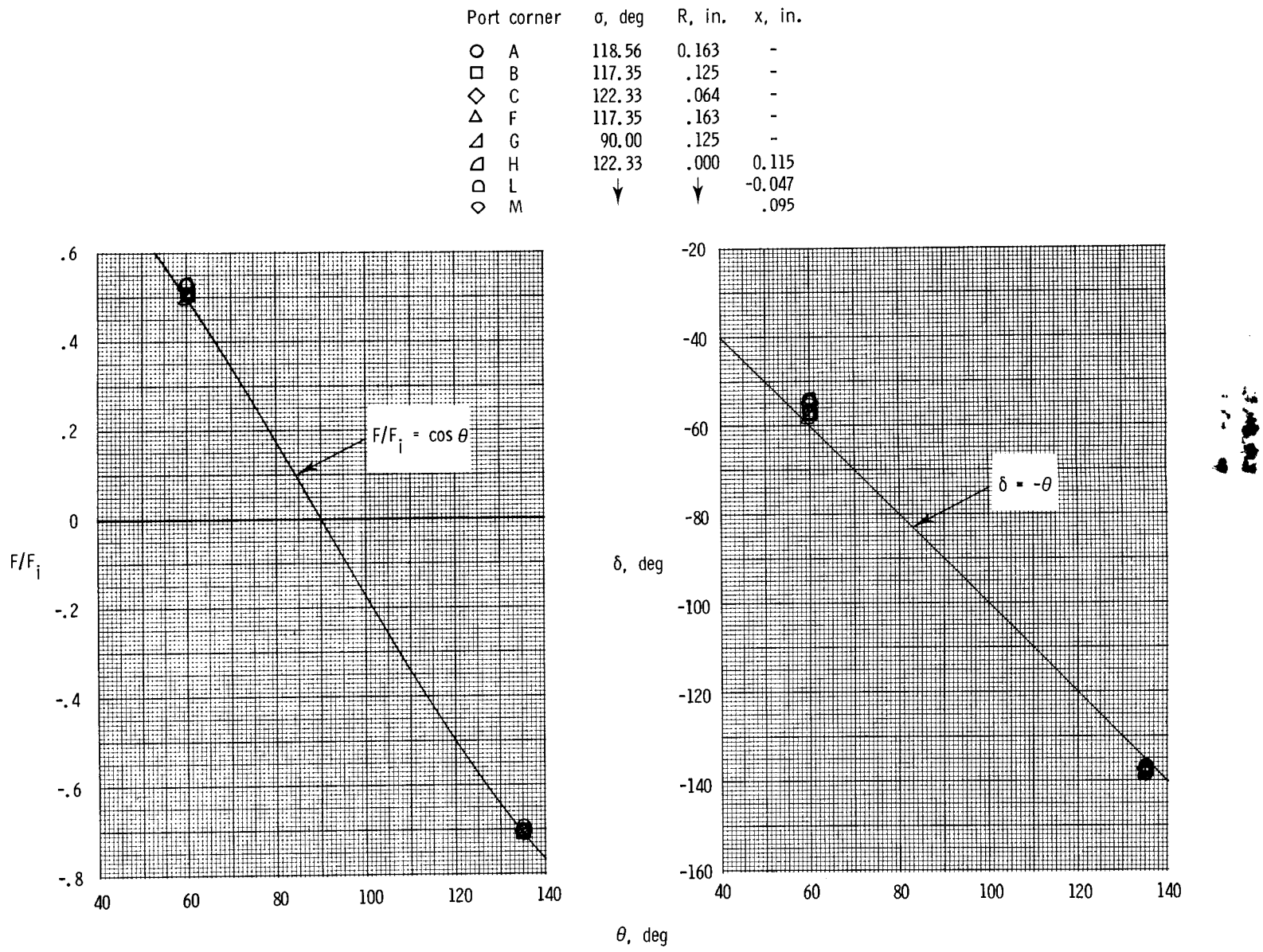

(c) NPR = 5.0.

Figure 13. Concluded.

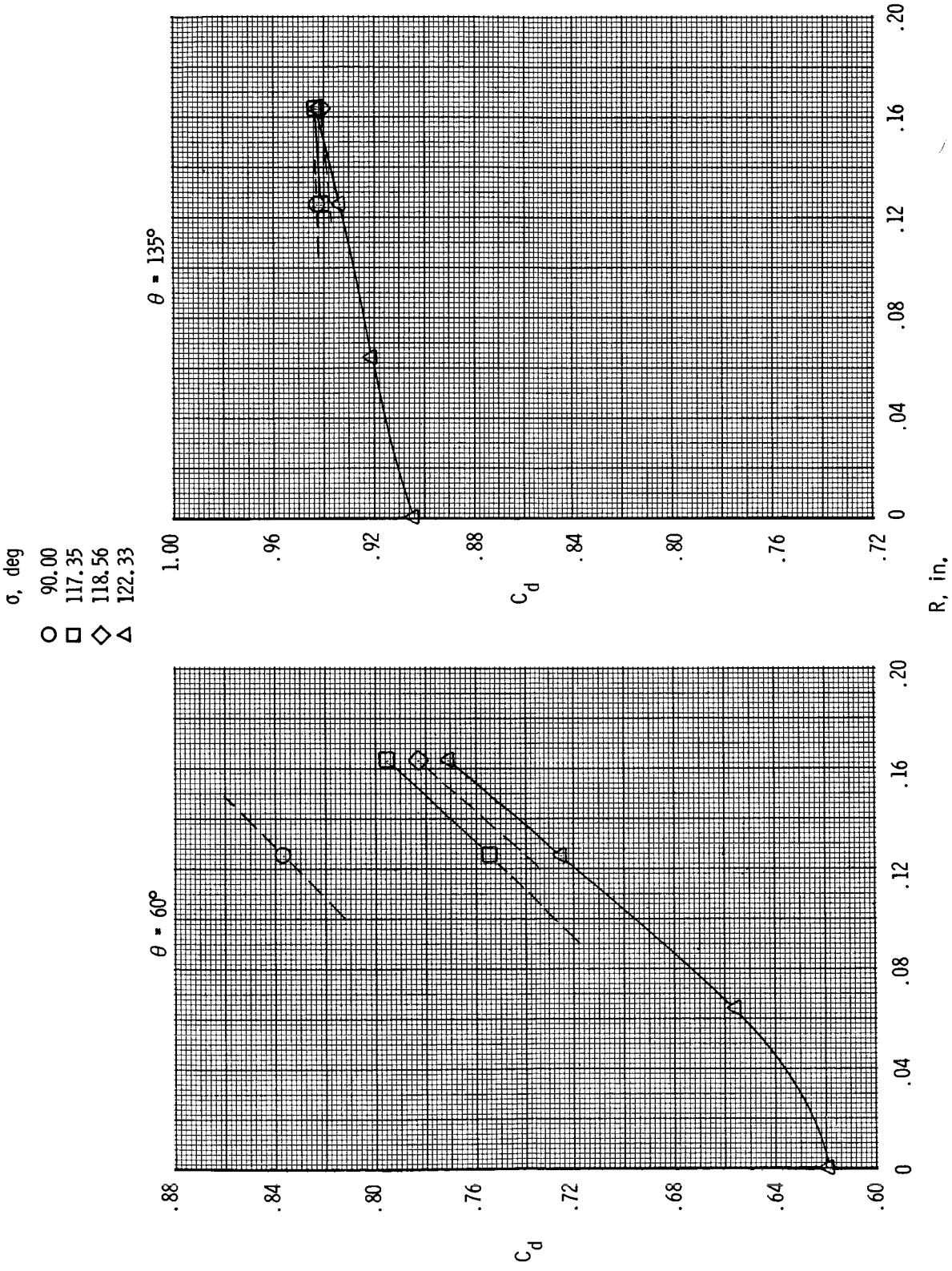

(a) NPR = 2.0.

Figure 14. Effect of upstream port corner angle and port corner radius of curvature on reverser discharge coefficient.

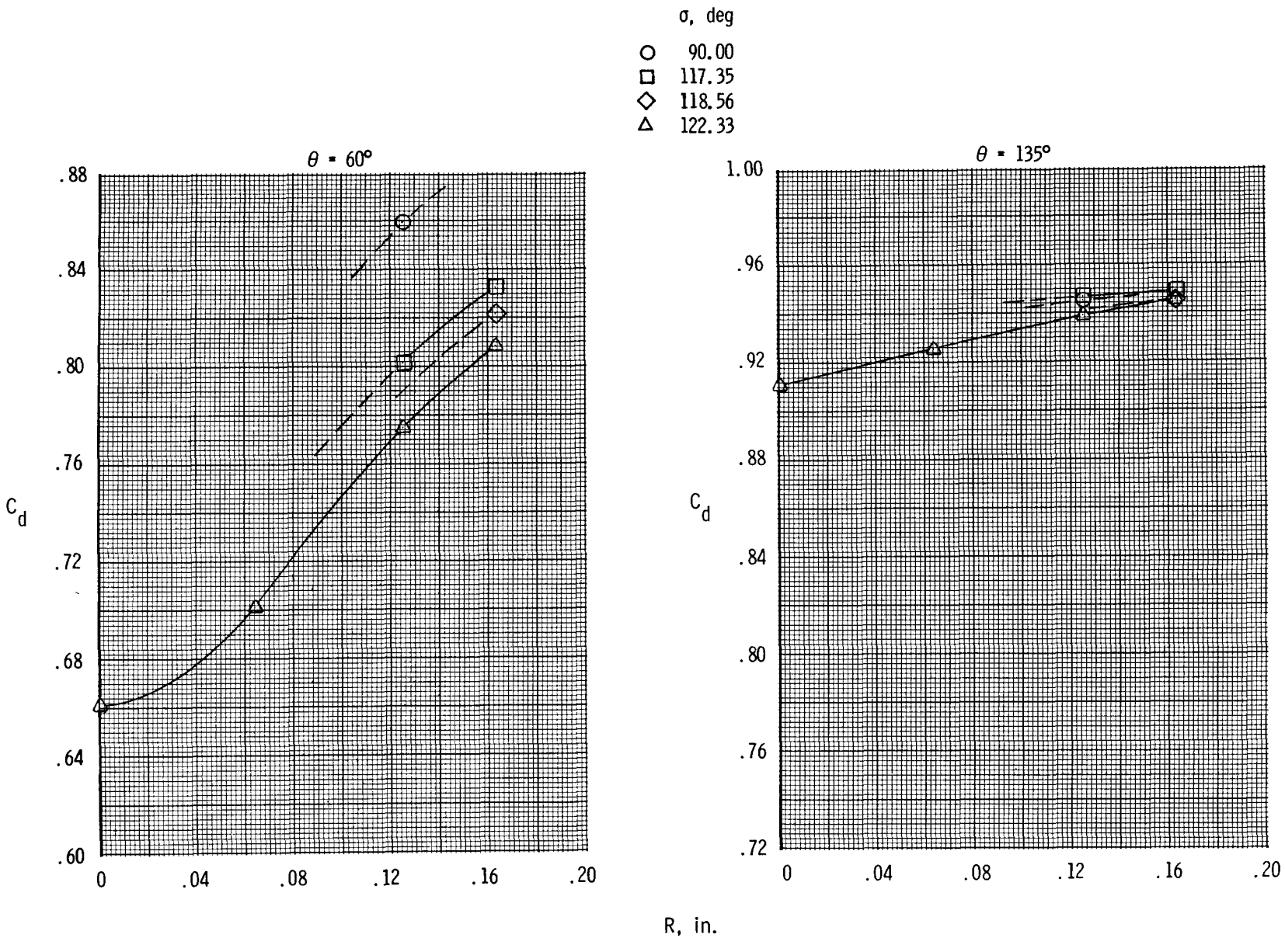

(b) NPR = 3.0.

Figure 14. Continued.

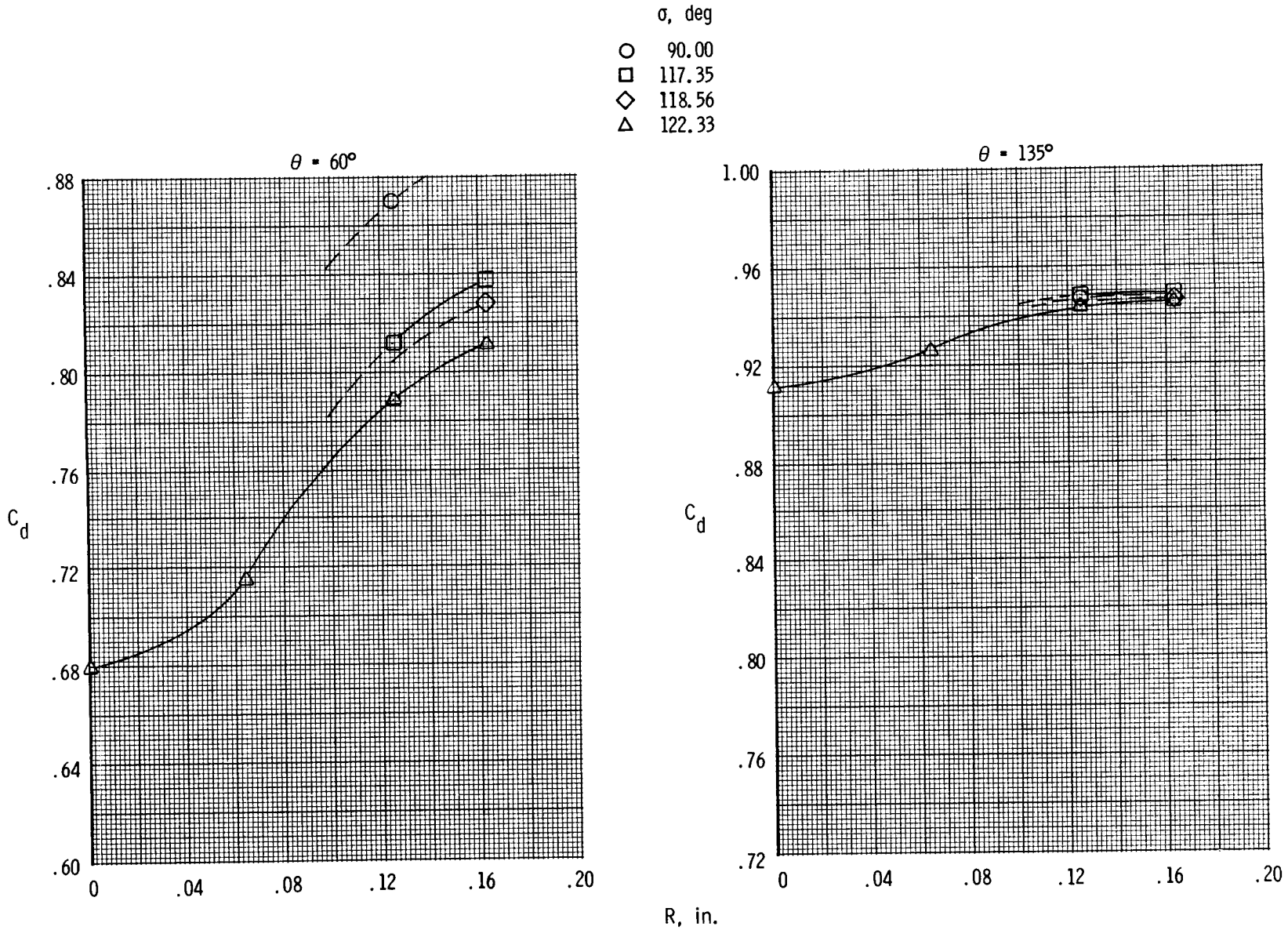

(c) NPR = 5.0.

Figure 14. Concluded.

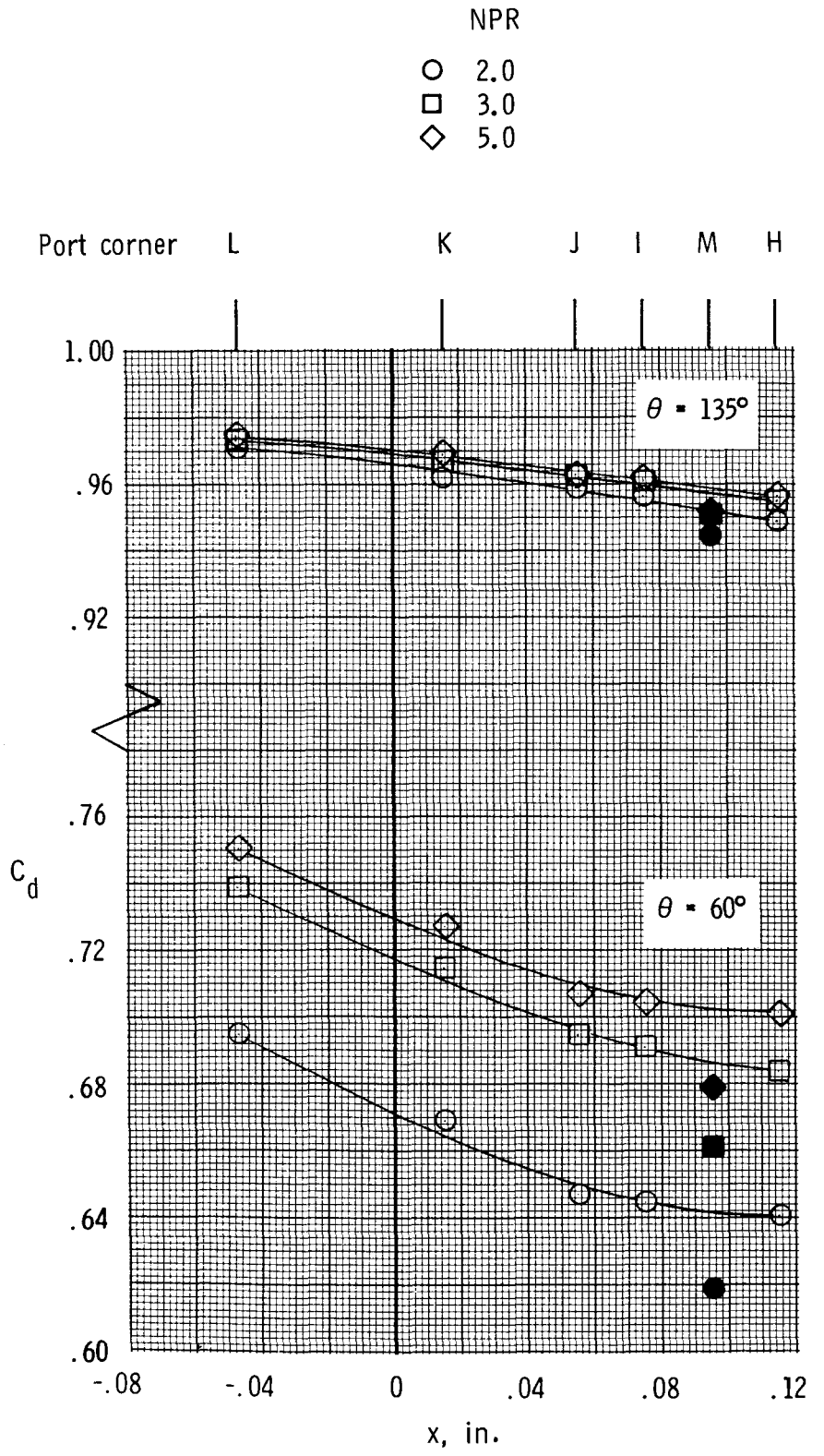

Figure 15. Effect of simulated cooling liner (blunt-base) location on reverser discharge coefficient. Solid symbols indicate angled base.

Standard Bibliographic Page

1. Report No.	2. Government Accession No.	3. Recipient's Catalog No.
NASA TP-2624		

4. Title and Subtitle	5. Report Date
Effect of Port Corner Geometry on the Internal Performance of a Rotating-Vane-Type Thrust Reverser	December 1986
	6. Performing Organization Code: 505-62-91-01
7. Author(s): Bobby L. Berrier and Francis J. Capone	8. Performing Organization Report No.: L-16135
9. Performing Organization Name and Address: NASA Langley Research Center, Hampton, VA 23665-5225	10. Work Unit No.
	11. Contract or Grant No.
12. Sponsoring Agency Name and Address: National Aeronautics and Space Administration, Washington, DC 20546-0001	13. Type of Report and Period Covered: Technical Paper
	14. Sponsoring Agency Code

15. Supplementary Notes

16. Abstract

An investigation has been conducted in the static-test facility of the Langley 16-Foot Transonic Tunnel to determine the effects of reverser port geometry on the internal performance of a nonaxisymmetric rotating-vane-type thrust reverser. Thrust reverser vane positions representing a spoiled-thrust (partially deployed) position and a full-reverse-thrust (fully deployed) position were tested with each port geometry variable. The effects of upstream port corner radius and wall angle on internal performance were determined. In addition, the effect of the length of a simulated cooling liner (blunt-base step) near the reverser port entrance was investigated; five different lengths were tested. All tests were conducted with no external flow, and nozzle pressure ratio was varied from 1.2 to 5.0.

17. Key Words (Suggested by Authors(s))	18. Distribution Statement
Thrust reverser Nonaxisymmetric nozzle Internal performance Discharge coefficient	Unclassified—Unlimited Subject Category 02

19. Security Classif.(of this report)	20. Security Classif.(of this page)	21. No. of Pages	22. Price
Unclassified	Unclassified	49	A03

For sale by the National Technical Information Service, Springfield, Virginia 22161

NASA-Langley, 1986